5-31-2021 2:00 PM

Investigating the Behavior of Adsorbed CO2 in Metal-Organic Frameworks via 13C Solid-state NMR Spectroscopy

Yingxian Li, *The University of Western Ontario*

Supervisor: Huang, Yining, *The University of Western Ontario*

A thesis submitted in partial fulfillment of the requirements for the Master of Science degree in Chemistry

Recommended Citation

Li, Yingxian, "Investigating the Behavior of Adsorbed CO2 in Metal-Organic Frameworks via 13C Solid-state NMR Spectroscopy" (2021). *Electronic Thesis and Dissertation Repository*. 7819.
https://ir.lib.uwo.ca/etd/7819

Abstract

Metal-organic frameworks (MOFs) are a class of microporous materials with lots of unique properties that make them promising candidates for carbon dioxide (CO_2) capture and storage. In this thesis, the adsorption behavior of CO_2 in MOF UTSA-74 (a framework isomer of a well-known MOF, MOF-74-Zn) is studied at a molecular level as it is a promising material for CO_2 storage. It has a distinct binuclear secondary building unit (SBU) that one of metal ions (Zn1) is in a tetrahedral coordination with no binding sites, while the other one (Zn2) is in an octahedral geometry with two open metal sites (OMSs) upon activation. Explicitly, variable temperature (VT) ^{13}C static solid-state nuclear magnetic resonance spectroscopy is used to investigate the behavior of $^{13}CO_2$ in UTSA-74 at low, moderate and high loading levels of $^{13}CO_2$ (i.e. 0.30, 0.54, 0.90 and 1.48 $^{13}CO_2$/ Zn2). The results reveal that all $^{13}CO_2$ molecules undergo localized wobbling. At low loading, some $^{13}CO_2$ molecules jump among three Zn2 OMSs in the cross-section of the channel, while others hop back and forth between the two neighbouring OMSs. At high loading, the three-site jumping has ceased, but two-site hopping persists. The dynamical behavior of $^{13}CO_2$ in UTSA-74 results from the unique Zn2 coordination environment. It was also discovered that $^{13}CO_2$ is less mobile in UTSA-74 than in its framework isomer, MOF-74-Zn.

Keywords

Gas adsorption, CO_2, host-guest interactions, metal-organic frameworks, MOFs, solid-state NMR, SSNMR, guest dynamics

Summary for Lay Audience

Metal-organic frameworks (MOFs), an emerging class of solid porous materials, have exhibited enormous potential for carbon dioxide (CO_2) capture and storage. In this thesis, MOF UTSA-74, a framework isomer of MOF-74, is studied as a promising material for CO_2 storage. It features a distinct binuclear secondary building unit (SBU) that one of metal ions (Zn1) is in a tetrahedral coordination with no binding sites, while the other one (Zn2) is in an octahedral geometry with two open metal sites (OMSs) upon activation. Therefore, UTSA-74 is structurally more advantageous than MOF-74-Zn because UTSA-74 has two binding sites available per Zn2 metal ion, whereas only one binding site is accessible per Zn ion in MOF-74-Zn. This extra binding site in UTSA-74 significantly enlarges the potential in gas adsorption capacities. In this thesis, the behavior of $^{13}CO_2$ in UTSA-74 at different $^{13}CO_2$ loading (low, moderate, high) levels are investigated by using variable-temperature (VT) ^{13}C static SSNMR spectroscopy because it offers the most direct insight into behavior of $^{13}CO_2$ within the framework as well as the guest-host interactions. The results reveal that all $^{13}CO_2$ molecules undergo localized wobbling around each Zn2 adsorption site. At low loading, some $^{13}CO_2$ molecules jump among three nonadjacent Zn2 OMSs in the cross-section of the channel, while others hop back and forth between the two neighbouring OMSs. At high loading, the three-site jumping has ceased, but two-site hopping persists. The dynamical behavior of $^{13}CO_2$ in UTSA-74 results from the unique Zn2 coordination environment. It was also discovered that $^{13}CO_2$ is less mobile in UTSA-74 than in its framework isomer, MOF-74-Zn.

Acknowledgments

It has been more than two years since the first day I started my M.Sc. degree in Western. Recalling the moment I received the offer, the first time I came to London, to Western, the first time I stepped into the chemistry building, to the lab and the first time I synthesized MOFs, these all seemed to happen yesterday as the inexpressible excitement felt the same when the flashback memories popped up in my mind. It has been so incredible that I have completed my master study and have harvested tremendous amount of memories along this journey. During these years, I have worked with so many excellent people who I would like to thank, indeed. Without their help, support and company, it would be impossible for me to complete my study successfully.

To begin with, I would like to show my most profound appreciation to my supervisor Dr. Yining Huang, for providing me with this precious opportunity to do research under his supervision at Western University, and for his encouragement throughout the research. He not only provided me numerous suggestions on my project, but also enlightened me as a mentor.

Next, it has been a great honour to work with the wonderful faculty and staff in the Department of Chemistry. I would like to firstly thank Dr. Mathew Willans, the NMR facility manager, for his instructions on NMR spectrometers. Whenever I need any technical support, no matter in experiments setup or data processing, he was always able to troubleshoot immediately and provided me valuable insights. Dr. Paul Boyle and Aneta Borecki have also offered me plenty of assistance in x-ray collection and data analysis. In addition, I would like to thank Ms. Janice Mathers, Ms. Sandy Holtslag, Mr. Naeem Shahid and Ms. Sue England for helping me complete the teaching assistant duties smoothly and enjoyably. Besides, a special thanks is given to Ms. Darlene McDonald, not only for her great help during my program, but also for her invaluable care at my tough time.

Moreover, I would also like to extend my appreciation to the members of my examination committee, Dr, John Corrigan and Dr. Lars Konermann for their advice on my first year report and for taking time to conduct my thesis examination.

Furthermore, I would like to thank the past and present members in my research group: Vinicius Martins, Sandamini Vidanalage, Ying-Tung Wong as well as my close friends in the Department of Chemistry: Brandon Yang, Ruizhong Zhang, Johnathan Wong, Kenneth Chu, who always hear me out, cheer me up and back me up. I have had so much cheerful time with them inside and outside of school, which makes my graduate life more relaxing.

Most importantly, I would like to express my greatest gratitude to my beloved parents for their unconditional love, faith and support. I am sincerely so grateful to have such open-minded parents, who always support me, trust me, respect my choices and let me be. In addition, I would like to thank my partner Jason Lee for being so supportive. He always enlarges my happiness but splits my sadness. Without him, it would not have been possible to finish my degree. Last but not least, I would love to thank my fluffy cat Bomi for being such a good kitty and for her company. She always sits next to the laptop whenever I am studying, while sometimes she does block the screen.

Table of Contents

List of Tables

List of Figures

List of Abbreviations

BDC	1,4-benzenedicarboxylate
CS	Chemical Shift
CSA	Chemical Shift Anisotropy
DMF	N, N-dimethylformamide
DI	Dipolar Interaction
DOBDC	2,5- dioxido-1,4 -benzenedicarboxylate
EXPRESS	Exchange program for relaxing spin systems
FID	Free Induction Decay
FT	Fourier Transformation
H_2BDC	benzene-1,4-dicarboxylic acid
H_4DOBDC	2,5-dihydroxy-1,4-benzenedicarboxylic acid
MAS	Magic Angle Spinning
MIL	Materials of the Institute Lavoisier
MOF	Metal-Organic Framework
NMR	Nuclear Magnetic Resonance
OMS	Open Metal Site
PAS	Principal Axis System
ppm	parts per million
pXRD	Powder X-Ray Diffraction
rf	Radio Frequency

SBU	Secondary Building Unit
S/N	Signal-to-Noise Ratio
SSNMR	Solid-State Nuclear Magnetic Resonance
TGA	Thermogravimetric analysis
TMS	Tetramethylsilane
VT	Variable Temperature

List of Appendices

Chapter 1

1 General introduction

1.1 Metal-organic frameworks (MOFs)

1.1.1 The threat of atmospheric carbon dioxide

Levels of CO_2, a significant atmospheric greenhouse gas, have increased rapidly in the past few centuries, leading to threatening climate change, namely global warming. According to the data from National Oceanic and Atmospheric Administration (NOAA), global mean CO_2 concentration was approximately 280 ppm[1] before the industrial revolution and hit another milestone targeting 415 ppm[2] as of May 2019 during solely two and half centuries (Figure 1-1).

The consequences of consistently climbing CO_2 concentration in the atmosphere are remarkable. To begin with, as the name suggests, global warming triggers worldwide elevated temperature. It was found that the average surface temperature has increased 0.9℃ since late 19th century, with majority of the warming having occurred in the past thirty-five years[3]. The trend was predicted to continue over the next century by rising 1.4℃ to 5.5℃[4]. It might seem insignificant, but it has strongly affected the daily life of humans as reflected by the frequency and intensity of extreme weathers including droughts, heat waves and floods, hurricanes etc. In addition, the occurrence of global warming triggers geological changes, for instance, sea levels rise, ice sheets melting and noticeable ocean acidification as 30% of atmospheric CO_2 could sink to ocean[5] as part of the carbon cycle. Taking ocean acidification as an example, when excess CO_2 dissolves in ocean, CO_2 reacts with seawater to form carbonic acid, a weak acid that acidifies the seawater, which further reacts with carbonate ions in the ocean, dissolves the significant compositions of marine animals such as shellfish and corals to make bicarbonate. In other words, with less carbonate ions present in water, those marine animals tend to build their shells thinner and more fragile, thus ocean acidification is regarded as a threatening factor for the subsistence of marine species. No matter from the standpoint of planetary warming, iceberg shrinking or the disruption of climate patterns, carbon cycle, continuous CO_2 increase is detrimental worldwide and minimizing CO_2 concentration is vital and needed.

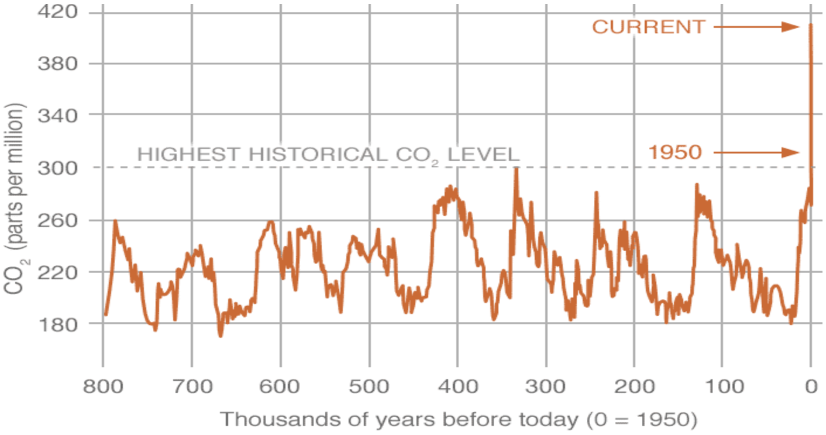

Figure 1-1: This graph demonstrates the atmospheric CO_2 level during the last three glacial cycles by measuring the atmospheric samples contained in ice cores and that from more recent direct measurements. It reveals that the atmospheric CO_2 has increased dramatically since the industrial revolution. (Reproduced from Ref. 6).

1.1.2 Carbon dioxide capture and storage

Conceptually, the reason why CO_2 levels increase is due to the difference between the rate of emission and the rate of absorption. Knowing the amount of CO_2 consistently increases over time, both natural and human activities contribute to the dramatical spike, while the latter factor takes greater proportion. This is because energy-driven fossil fuel consumption is indispensable to meet daily demands in various perspectives, which include but not limited to electricity production, industrial or agricultural use and transportation. Transportation is the leading contributor that makes up nearly 29% of carbon dioxide emission, followed by electricity generation with 27.5% and industry operation with 22%[7]. Being aware of the great CO_2 emission from burning natural gas, petroleum and coals, it is highly impending to figure out approaches to resolve or slow down the dilemma. Substituting to less carbon-intensive fuels, renewable energy sources, such as wind and solar energy, improving the efficiency of fossil-powered power plants from the originating source or capturing CO_2 before it transports to the atmosphere are possible solutions broadly seen. It is worth mentioning that designing specific materials for CO_2 capture and fuel storage is a desired and promising approach to slow down or stop the downside of anthropogenic CO_2.

Admittedly, the exploration towards potential CO_2 adsorption materials is ceaseless, which includes traditional CO_2 adsorbents such as aqueous alkanolamine solutions, zeolites, activated carbon and more newly studied materials like metal-organic frameworks (MOFs). It has been many decades since aqueous alkanolamine solutions were implemented for CO_2 captures and they are still considered as the standard in terms of the adsorption performance. Typically, aqueous alkanolamine solutions, for instance, monoethanolamide (MEA) and triethanolamine (TEA) interact with CO_2 to form carbamate or bicarbonate species, respectively as shown in Figure 1-2 and the affinity of these solutions towards CO_2 capture is considered exceptional[8]. However, the strong capability in trapping CO_2, at the same time, is a double-edged sword because if the interaction is exceedingly tight, it means a high energy is required to desorb CO_2. Moreover, aqueous alkanolamine solutions are highly corrosive, notably unstable under heat and readily decompose over time; such factors act to reduce their lifespan and allure as adsorbents in industry[8]. Zeolites are extensively studied porous aluminosilicate materials for CO_2 capture, possessing high chemical and thermal stability; such is demonstrated by their structural integrity under high temperatures. Besides, they also feature more rapid CO_2 adsorption and lower adsorption energy penalty than aqueous alkanolamine adsorbents because of their much lower heat capacities, which is significant in reducing the regeneration energy[8]. However, zeolites get saturated with water vapour from the flue gas stream easily, which restricts the adsorption capacity and the CO_2 desorption process requires high temperature, which hinders the desorption of the captured CO_2[8]. Activated carbons, another representative solid porous CO_2 adsorbents, are advantageous of extraordinarily high surface area, which gives rise to high adsorption capacities at high pressures, thus making them excellent candidates in high-pressure gas separation applications[8]. The hydrophobic properties of activated carbons also diminish the negative impacts from water vapour, which broaden their uses in hydrated environment since their capacities and lifespans are not influenced as greatly as other adsorbent materials like zeolites. Nevertheless, activated carbons have much lower CO_2 capacities at low pressures, which restrict the industrial practice[8]. In addition to these conventional adsorbent materials, MOFs are considered as the new-era novel class of porous solid CO_2 adsorbents.

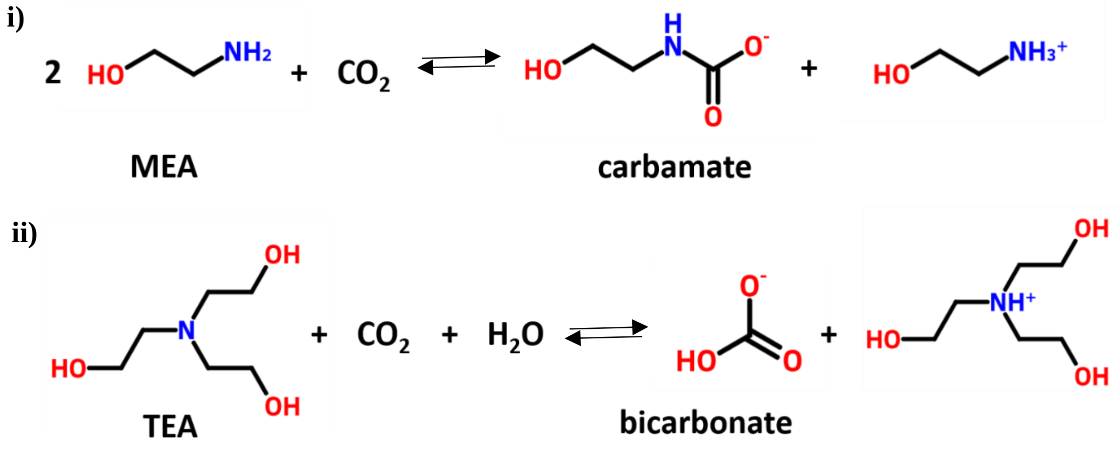

Figure 1-2: The reactions of CO_2 with i) monoethanolamide (MEA) and ii) triethanolamine (TEA), resulting in an anionic carbamate species and a bicarbonate species, correspondingly. (Reproduced from Ref. 8).

1.1.3 Composition and properties of MOFs

Metal-organic frameworks[9], a type of emerging materials that have been extensively studied in the last two decades such as MOF-74-Zn[10], MIL-53-Al[11], have many potential applications in gas storage[12-14], separation[12,15-18], adsorption[15], catalysis[19-21] and drug delivery[22,23] etc. In general, MOFs are porous organic-inorganic hybrid structures formed by self-assembled metal cations or clusters and organic linkers to form three-dimensional frameworks with voids (Figure 1-3)[24], typically prepared by hydrothermal synthesis method, which is the most commonly used approach in MOFs synthesis. The integration of metal cations connected organic linkers lead to a remarkably organized structure with permanent porosity.

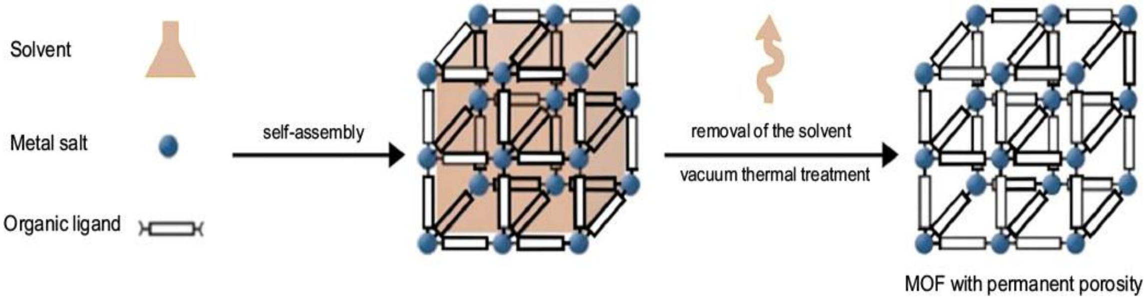

Figure 1-3: Schematic diagram of basic composition of metal-organic frameworks, followed by the removal of solvent molecules. (Reproduced from Ref. 24).

Generically, MOF synthesis methods can be categorized into two classes: solvothermal and non-solvothermal[25]. As the name implies, solvothermal methods use solvents in the synthesis process, which is usually carried out at or above the boiling temperature of the solvents in closed chemical reactors at elevated pressure[25]. When water is used in the synthesis, the method is also known as hydrothermal synthesis. Conversely, typical non-solvothermal methods that include microwave synthesis, electrochemical synthesis, mechanochemical synthesis and sonochemical synthesis do not require closed chemical reactors or high temperature and can be conducted at room temperature or on heating in open flasks at atmospheric pressure[25]. Because of the elevated pressure and temperature in the solvothermal synthesis, the solubility of salts is exceedingly improved, which in turn promotes the nucleation reaction, giving rise to better yields and crystallinity.

Taking MIL-53-Al as an example, MIL-53-Al is a MOF that was extensively studied and exhibits strong CO_2 adsorption affinities. It was synthesized by mixing aluminum nitrate nonahydrate $Al(NO_3)_3·9H_2O$, benzene-1,4-dicarboxylic acid (H_2BDC) ligands in deionized H_2O in a Teflon-lined stainless steel autoclave at 220℃ for 72 hours. The secondary building unit (SBU) of MIL-53-Al is $AlO_4(OH)_2$, which is composed of an Al metal center connected to four oxygens from four BDC linkers and two bridging hydroxyl oxygen atoms. The bridging hydroxyl oxygens link SBUs to form an indefinite chain and these chains are further interconnected by BDC linkers to create rhombic channels (Figure 1-4).

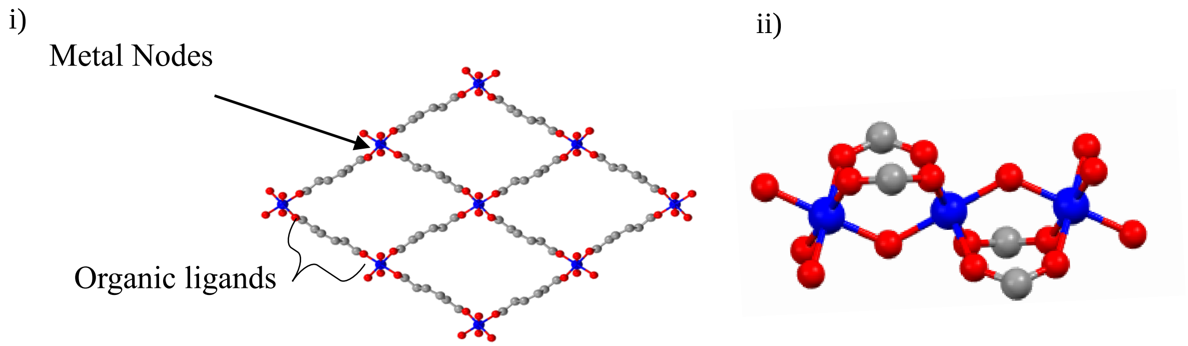

Figure 1-4: i) Schematic illustration of the composition of MIL-53-Al ii) MIL-53-Al secondary building unit connections. Atom colors: Al-Blue, O-Red, C-Grey.

Characteristically, MOFs are the materials with unique properties such as exceptional porosity, large surface area, high thermal stability and variability. The porosity of MOFs can be modified by varying the integration of inorganic metal cations and organic linkers. Typically, MOFs with high porosity pair with long organic linkers, whereas those with low porosity usually come with short organic linkers[24], as seen in Figure 1-5. The surface areas of MOFs are mostly hundreds to thousands of m^2/g, which are exceedingly high relative to conventional adsorbents[26] and are considered significant in enhancing CO_2 capacities. Furthermore, because strong bonds, for instance, C-O, C-C, M-O are the main components in the MOFs frameworks, they feature MOFs high thermal stability. Variability is also one of the stunning features of MOFs. By varying the internal and external factors, endless MOFs can be designed, such as the following: 1) The selection of metal elements. Different metal cations have various charges and coordination numbers, which depend on the intrinsic nature of the metal centers. By substituting to different metal cations, a large variety of MOFs can be synthesized, capable for different applications. 2) The selection of organic linkers. The length and complexity of organic linkers, which can be further altered by introducing functional groups such as -OH, -Cl, $-NH_2$, substantially determine the size of MOFs pores and limit the accessibility of guest molecules. This in turn promotes the potential applications in gas selectivity and separation[8,27-30]. In addition, the variety of organic linkers also affects the location and the strength of interactions between guest molecules and adsorption sites. 3) The selection of solvents. As a number of MOFs are H_2O-sensitive, it is very important to pick proper solvents or prepare solvents at a precise ratio when more than one solvent is used in synthesis. Besides, if the size of solvents is smaller than the size of pores, an extra step of solvent-exchange is required to remove solvent molecules from the pores post synthesis. 4) The selection of synthesis conditions. Synthesis conditions such as temperature and synthesis time are highly important since they can possibly lead to the formation of different congeners or polymorphs even though from the same synthesis mixture[31]. For example, MIL-101-Cr will be converted to MIL-53-Cr by elongating the synthesis time. It was observed that MIL-101-Cr is degraded at longer synthesis time and the decomposed species, in consequence, are reorganized to form MIL-53-Cr[32].

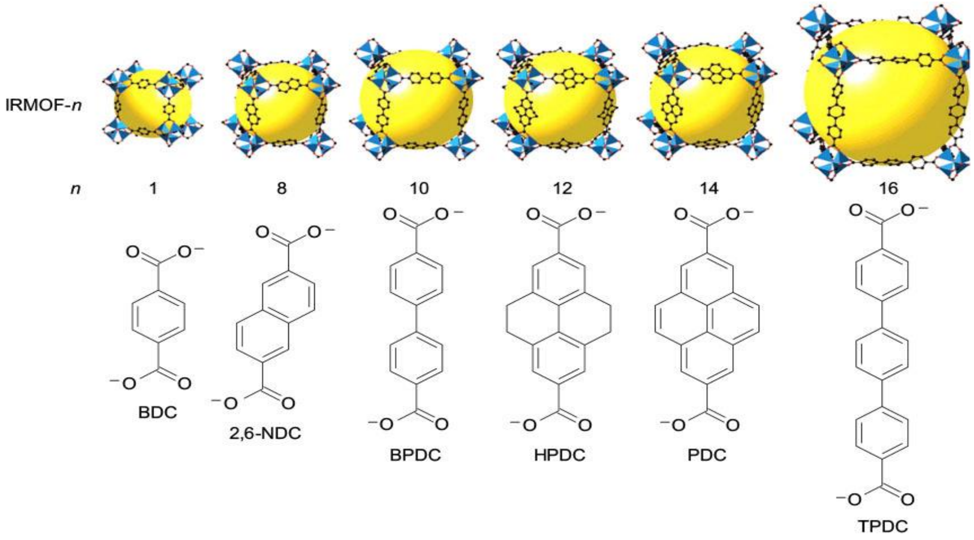

Figure 1-5: The derivates of IRMOF-n incorporating various kinds of organic linkers, leading to MOFs with different porosity. The yellow color sphere indicates the open pore space that is accessible to e.g. gas molecules or solvents. It is clearly shown that longer linkers give rise to larger porosity. (Reproduced from Ref. 24).

1.1.4 MOFs studied in the thesis

Knowing that MOFs are a new-generation material in trapping post-combustion CO_2, it is desirable to investigate MOFs with potentially CO_2 adsorption capacities. Thus, UTSA-74 is chosen as a candidate for this thesis.

UTSA-74 is a MOF that was firstly synthesized in 2016 by Luo et al.[33] as an isomer of a more well-known porous material called MOF-74-Zn[10], which is also known as CPO-27-Zn. Structurally, MOF-74-Zn is characteristic of one-dimensional hexagonal channels that are formed by edge-sharing octahedrally-coordinated Zn^{2+} metal ions with interlinking 2,5-dioxido-1,4-benzenedicarboxylate (DOBDC) linkers (Figure 1-6).

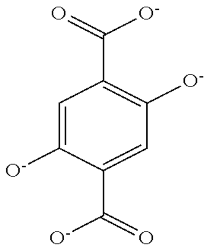

Figure 1-6: Structure of DOBDC linker.

The framework structure of MOF-74-Zn, as viewed along the crystallographic c-axis, is shown in Figure 1-7i. The crystal structure is rhombohedral and the space group is $R\bar{3}$[34]. In MOF-74, each Zn ion is connected to three DOBDC carboxylate oxygen atoms, two DOBDC hydroxyl oxygen atoms and one unsaturated binding site for the guest molecules (Figure 1-7i). MOF-74 has the highest open metal site (OMS) densities by far[33], giving rise to highest CO_2 adsorption capacity among MOFs. MOF-74-Mg[35,36] and MOF-74-Zn[10] can adsorb up to 162 cm^3/cm^3 and 146 cm^3/cm^3 of CO_2, respectively. Framework isomers, by definition, are the MOFs that are constructed from the identical metal ions and ligands but have different interconnecting frameworks and properties presumably by varying synthesis time length or temperature[37]. In this case, UTSA-74 is generated when synthesis temperature is increased to 158 °C instead of 105 °C[10,33]. UTSA-74 crystallizes in $R\bar{3}c$ space group and also exhibits one-dimensional channels along the c-direction[33](Figure 1-7ii). Nevertheless, unlike the uniform rod-packing structure in MOF-74-Zn, the binuclear secondary building units (SBU) brought up the unique composition of dual channel system with different Zn^{2+} sites. The first Zn metal site (Zn1) is saturated and tetrahedrally coordinated by connecting to two DOBDC carboxylate oxygen atoms as well as two DOBDC hydroxyl oxygen atoms, whereas the second metal site (Zn2) is octahedrally linked to four DOBDC oxygen atoms plus two terminal coordinated solvent molecules, which can be removed after high-temperature activation, creating two vacant sites in axial orientation for two gas molecules binding to the pore surfaces (Figure 1-7ii). The unique topology of UTSA-74 has one-dimensional channels with pore size 8Å, which is smaller than that of Zn-MOF-74 with 11Å.

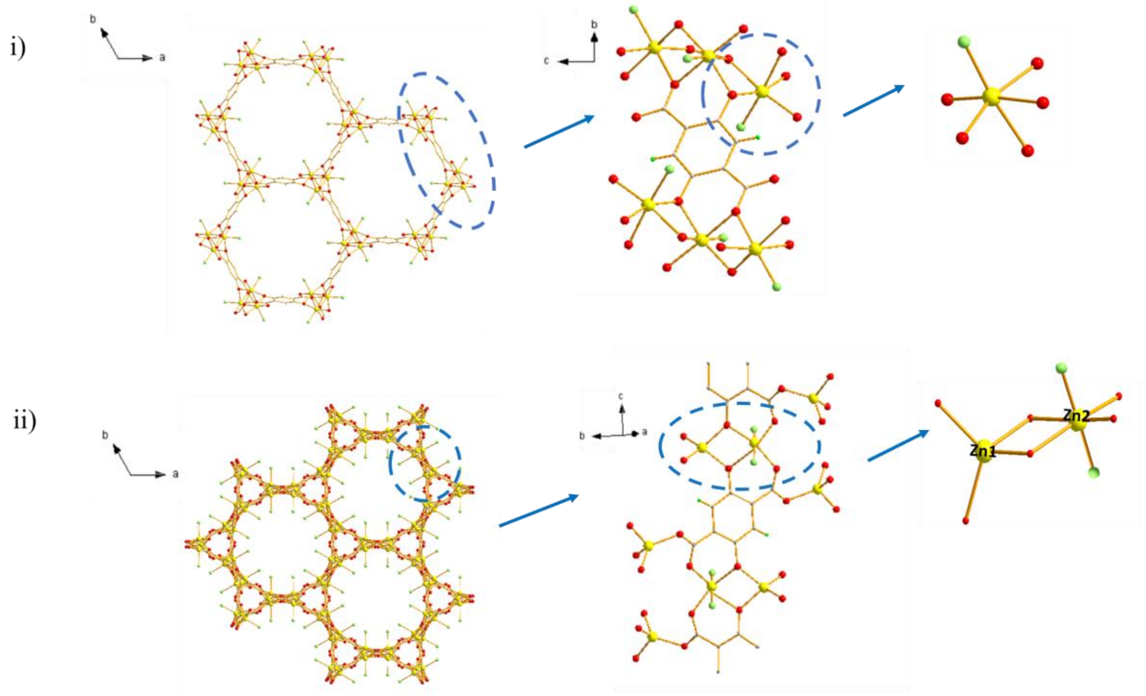

Figure 1-7: i) Structures of MOF-74-Zn. ii) UTSA-74. The unique composition of dual channel system in UTSA-74 provides two available binding sites per SBU for guest molecules, which is more advantageous than MOF-74-Zn as each Zn ion in MOF-74-Zn can only bind to one guest molecule. This extra binding site in UTSA-74 significantly enlarges the potential in gas adsorption capacities. Atom colors: Zn-Yellow, O-Red, C-Grey, Guest Molecules-Green.

1.2 Outline of the thesis

Persistently climbing atmospheric CO_2 concentrations and temperatures (i.e. global warming) have been disconcerting world-widely, primarily due to the large amount of emission from anthropogenic CO_2. Thus, it is essential to reduce the CO_2 in the atmosphere and capturing CO_2 by solid porous materials is considered one of the promising approaches. MOFs, as a class of new-era solid porous CO_2 adsorbents, which exhibit exceptional porosity, surface area, thermal stability and variability, have been studied extensively in trapping post-combustion CO_2. In this thesis, UTSA-74, an isomer of MOF-74, which has unique composition of dual channel system, is chosen as the promising candidate. Studying the motions of CO_2 inside the framework and the interactions between CO_2 and UTSA-74 framework allows us to apprehend how the unique dual channel of UTSA-74 benefits the CO_2 adsorption. Variable-temperature (VT) ^{13}C static SSNMR spectroscopy is employed as the characterization technique as it offers the most direct insight into the dynamics and adsorptive behavior within the framework as well as the guest-host interactions. By means of analytical and dynamical simulation software, i.e. WSolids and EXPRESS, NMR parameters such as isotropic chemical shift, span, skew and the CO_2 motional modes including motional types, rates and rotation angles of adsorbed CO_2 molecules associated with the binding sites at different temperatures can be obtained.

A total of four chapters are included in this thesis. In chapter 1, a general introduction of the metal-organic frameworks is given. Chapter 2 mainly focuses on the physical and experimental background of solid-state NMR. In chapter 3, the adsorptive properties and dynamic behavior of isotopically-labeled $^{13}CO_2$ in UTSA-74 at various loading levels i.e. 0.30, 0.54, 0.90 and 1.48 CO_2/ Zn2 are examined using static VT ^{13}C static NMR spectroscopy. Chapter 4 is the last chapter, which is composed of a brief summary of the thesis and a short description of future works.

1.3 Bibliography

1. CO_2 at NOAA's Mauna Loa Observatory Reaches New Milestone: Tops 400 ppm. https://www.esrl.noaa.gov/gmd/news/7074.html (accessed Aug 20, **2019**).
2. Harvey, C; E & E News. CO_2 Levels Just Hit Another Record—Here's Why It Matters. https://www.scientificamerican.com/article/CO2-levels-just-hit-another-record-heres-why-it-matters/ (accessed Aug 20, **2019**).
3. Climate Change Evidence: How Do We Know? https://climate.nasa.gov/evidence/ (accessed Aug 20, **2019**).

4. The Effects of Climate Change. https://climate.nasa.gov/effects/ (accessed Aug 20, **2019**).
5. Effects of Changing the Carbon Cycle. https://earthobservatory.nasa.gov/features/CarbonCycle/page5.php (accessed Aug 25, **2019**).
6. Carbon Dioxide Concentration. https://climate.nasa.gov/vital-signs/carbon-dioxide/ (accessed Dec **2020**).
7. Sources of Greenhouse Gas Emissions. https://www.epa.gov/ghgemissions/sources-greenhouse-gas-emissions (accessed Aug 25, **2019**).
8. Sumida, K.; Rogow, D. L.; Mason, J. A.; Mcdonald, T. M.; Bloch, E. D.; Herm, Z. R.; Bae, T.-H.; Long, J. R. Carbon Dioxide Capture in Metal–Organic Frameworks. *Chemical Reviews* **2011**, *112* (2), 724–781.
9. Yaghi, O. M.; Li, H. L., Hydrothermal Synthesis of a Metal-Organic Framework Containing Large Rectangular Channels. *Journal of the American Chemical Society* **1995**, *117* (41), 10401-10402.
10. Rosi, N. L.; Kim, J.; Eddaoudi, M.; Chen, B.; O'Keeffe, M.; Yaghi, O. M. Rod Packings and Metal−Organic Frameworks Constructed from Rod-Shaped Secondary Building Units. *Journal of the American Chemical Society* **2005**, *127* (5), 1504–1518.
11. Loiseau, T.; Serre, C.; Huguenard, C.; Fink, G.; Taulelle, F.; Henry, M.; Bataille, T.; Férey, G. A Rationale for the Large Breathing of the Porous Aluminum Terephthalate (MIL-53) Upon Hydration. *Chemistry - A European Journal* **2004**, *10* (6), 1373–1382.
12. Li, B.; Wen, H.-M.; Zhou, W.; Chen, B. Porous Metal–Organic Frameworks for Gas Storage and Separation: What, How, and Why? *The Journal of Physical Chemistry Letters* **2014**, *5* (20), 3468–3479.
13. Ma, S, Zhou, H-C. Gas Storage in Porous Metal-Organic Frameworks for Clean Energy Applications. *Chemical Communications* **2010**, 46(1): 44–53.
14. Millward, A. R.; Yaghi, O. M. Metal−Organic Frameworks with Exceptionally High Capacity for Storage of Carbon Dioxide at Room Temperature. *Journal of the American Chemical Society* **2005**, *127* (51), 17998–17999.
15. Li, J.-R.; Kuppler, R. J.; Zhou, H.-C., Selective Gas Adsorption and Separation in Metal–Organic Frameworks. *Chemical Society Reviews* **2009,** *38* (5), 1477-1504.
16. Li, J.-R.; Sculley, J.; Zhou, H.-C. Metal–Organic Frameworks for Separations. *Chemical Reviews* **2011**, *112* (2), 869–932.
17. Nugent, P.; Belmabkhout, Y.; Burd, S. D.; Cairns, A. J.; Luebke, R.; Forrest, K.; Pham, T.; Ma, S.; Space, B.; Wojtas, L.; Eddaoudi, M.; Zaworotko, M. J. Porous Materials with Optimal Adsorption Thermodynamics and Kinetics for CO_2 Separation. *Nature* **2013**, *495* (7439), 80–84.
18. Liu, X.-T.; Jia, Y.-Y.; Zhang, Y.-H.; Ren, G.-J.; Feng, R.; Zhang, S.-Y.; Zaworotko, M. J.; Bu, X.-H. A New Co(II) Metal–Organic Framework with Enhanced CO_2

Adsorption and Separation Performance. *Inorganic Chemistry Frontiers* **2016**, *3* (12), 1510–1515.

19. Liu, J.; Chen, L.; Cui, H.; Zhang, J.; Zhang, L.; Su, C.-Y. Applications of Metal–Organic Frameworks in Heterogeneous Supramolecular Catalysis. *Chemical Society Reviews* **2014**, *43* (16), 6011–6061.
20. Lee, J.; Farha, O. K.; Roberts, J.; Scheidt, K. A.; Nguyen, S. T.; Hupp, J. T., Metal–Organic Framework Materials as Catalysts. *Chemical Society Reviews* **2009,** *38* (5), 1450-1459.
21. Dhakshinamoorthy, A.; Garcia, H. Catalysis by Metal Nanoparticles Embedded on Metal–Organic Frameworks. *Chemical Society Reviews* **2012**, *41* (15), 5262.
22. Horcajada, P.; Chalati, T.; Serre, C.; Gillet, B.; Sebrie, C.; Baati, T.; Eubank, J. F.; Heurtaux, D.; Clayette, P.; Kreuz, C.; Chang, J.-S.; Hwang, Y. K.; Marsaud, V.; Bories, P.-N.; Cynober, L.; Gil, S.; Férey, G.; Couvreur, P.; Gref, R. Porous Metal–Organic-Framework Nanoscale Carriers as a Potential Platform for Drug Delivery and Imaging. *Nature Materials* **2009**, *9* (2), 172–178.
23. Horcajada, P.; Serre, C.; Vallet-Regí, M.; Sebban, M.; Taulelle, F.; Férey, G. Metal–Organic Frameworks as Efficient Materials for Drug Delivery. *Angewandte Chemie International Edition* **2006**, *45* (36), 5974–5978.
24. Tsivadze, A. Y.; Aksyutin, O. E.; Ishkov, A. G.; Knyazeva, M. K.; Solovtsova, O. V.; Men'shchikov, I. E.; Fomkin, A. A.; Shkolin, A. V.; Khozina, E. V.; Grachev, V. A. Metal-Organic Framework Structures: Adsorbents for Natural Gas Storage. *Russian Chemical Reviews* **2019**, *88* (9), 925–978.
25. Butova, V. V.; Soldatov, M. A.; Guda, A. A.; Lomachenko, K. A.; Lamberti, C. Metal-Organic Frameworks: Structure, Properties, Methods of Synthesis and Characterization. *Russian Chemical Reviews* **2016**, *85* (3), 280–307.
26. Furukawa, H.; Cordova, K. E.; O’Keeffe, M.; Yaghi, O. M. The Chemistry and Applications of Metal-Organic Frameworks. *Science* **2013**, *341* (6149), 1230444.
27. Stavitski, E.; Pidko, E. A.; Couck, S.; Remy, T.; Hensen, E. J.; Weckhuysen, B. M.; Denayer, J.; Gascon, J.; Kapteijn, F. Complexity behind CO_2 Capture on NH_2-MIL-53(Al). *Langmuir* **2011**, *27* (7), 3970–3976.
28. Zhang, Z.; Yao, Z.-Z.; Xiang, S.; Chen, B. Perspective of Microporous Metal–Organic Frameworks for CO_2 Capture and Separation. *Energy & Environmental Science* **2014**, *7* (9), 2868.
29. Torrisi, A.; Bell, R. G.; Mellot-Draznieks, C. Functionalized MOFs for Enhanced CO_2 Capture. *Crystal Growth & Design* **2010**, *10* (7), 2839–2841.
30. Devic, T.; Horcajada, P.; Serre, C.; Salles, F.; Maurin, G.; Moulin Béatrice; Heurtaux, D.; Clet, G.; Vimont, A.; Grenèche Jean-Marc; Ouay, B. L.; Moreau, F.; Magnier, E.; Filinchuk, Y.; Marrot Jerôme; Lavalley, J.-C.; Daturi, M.; Férey Gérard. Functionalization in Flexible Porous Solids: Effects on the Pore Opening and the

Host−Guest Interactions. *Journal of the American Chemical Society* **2010**, *132* (3), 1127–1136.

31. Bueken, B.; Reinsch, H.; Heidenreich, N.; Vandekerkhove, A.; Vermoortele, F.; Kirschhock, C. E. A.; Stock, N.; Vos, D. D.; Ameloot, R. An in Situ Investigation of the Water-Induced Phase Transformation of UTSA-74 to MOF-74(Zn). *CrystEngComm* **2017**, *19* (29), 4152–4156.
32. Khan, N. A.; Jhung, S. H. Phase-Transition and Phase-Selective Synthesis of Porous Chromium-Benzenedicarboxylates. *Crystal Growth & Design* **2010**, *10* (4), 1860–1865.
33. Luo, F.; Yan, C.; Dang, L.; Krishna, R.; Zhou, W.; Wu, H.; Dong, X.; Han, Y.; Hu, T.-L.; O'Keeffe, M.; Wang, L.; Luo, M.; Lin, R.-B.; Chen, B. UTSA-74: A MOF-74 Isomer with Two Accessible Binding Sites per Metal Center for Highly Selective Gas Separation. *Journal of the American Chemical Society* **2016**, *138* (17), 5678–5684.
34. González-Galán, C.; Balestra, S. R.; Luna-Triguero, A.; Madero-Castro, R. M.; Zaderenko, A. P.; Calero, S. Effect of Diol Isomer/Water Mixtures on the Stability of Zn-MOF-74. *Dalton Transactions* **2021**, *50* (5), 1808–1815.
35. Dietzel, P. D. C.; Blom, R.; Fjellvåg, H. Base-Induced Formation of Two Magnesium Metal-Organic Framework Compounds with a Bifunctional Tetratopic Ligand. *European Journal of Inorganic Chemistry* **2008**, *2008* (23), 3624–3632.
36. Xiang, S.; He, Y.; Zhang, Z.; Wu, H.; Zhou, W.; Krishna, R.; Chen, B. Microporous Metal-Organic Framework with Potential for Carbon Dioxide Capture at Ambient Conditions. *Nature Communications* **2012**, *3* (1).
37. Makal, T. A.; Yakovenko, A. A.; Zhou, H.-C. Isomerism in Metal–Organic Frameworks: "Framework Isomers." *The Journal of Physical Chemistry Letters* **2011**, *2* (14), 1682–1689.

Chapter 2

2 Introduction of solid-state nuclear magnetic resonance (SSNMR)

2.1 Physical Background

In order to characterize the synthesized MOFs, understand the structure and local interactions with guest molecules, a few methods can be employed for characterization. powder X-ray diffraction (pXRD) and solid-state nuclear magnetic resonance (SSNMR) are typical characterization approaches used in my lab group.

SSNMR is regarded as one of the most powerful methods for materials characterization. Specifically, it is used to examine the local environments of nuclei in materials of interest[1,2]. SSNMR probes short-ranged local structural, magnetic, electronic surrounding of target nuclei and can reveal the dynamics information and behavior of adsorbed gases in crystalline materials, such as MOFs and amorphous materials.

For SSNMR, two factors are important: nuclei spins (I)[3] and an applied magnetic field (B_0)[4,5]. In order to be magnetically active, a nucleus must have a non-zero nuclear spin quantum number ($I \neq 0$), which requires an odd number in either protons or neutrons of nucleus, though $I = {}^{1}/_{2}$ is preferable in order to have a spherical distribution of charges. The established guideline to predict nuclear spin quantum number I is listed in Table 2-1.

Table 2-1: The guideline to predict spin quantum number *I*.

Number of protons	**Number of neutrons**	**Spin**	**Example**
Even	Even	Zero	^{12}C
Even	Odd	Half-integer (i.e. ${}^{1}/_{2}$)	^{13}C
Odd	Even	Half-integer (i.e. ${}^{3}/_{2}$)	^{7}Li
Odd	Odd	Integer (i.e. 1)	^{2}H

2.1.1 Zeeman interaction

When a nucleus with a spin is put in an external magnetic field such as the magnet of an NMR spectrometer, the magnetic moment (μ)[4] of the nucleus, which has a linear relationship with spins that $\mu = \gamma I$, will behave as a bar magnet that interacts with the main magnetic field, responsible for the initial splitting to $2I+1$ energy levels, which is known as Zeeman interaction[4,5]. The number of energy levels is defined by magnetic quantum number (m_I), ranging from I, I-1 to -I+1, -I. In other words, in the absence of external magnetic field B_0, $2I+1$ energy levels are degenerate, while in the presence of B_0, these energy levels are non-equivalent and split. As demonstrated in Figure 2-1, after a spin-1/2 nucleus is placed in the external magnetic field, the degenerate energy levels split into two energy levels, which corresponds to two nuclear spin states m_I= -1/2 and m_I=1/2, where m_I=-1/2 is the higher energy state that aligns against B_0 and conversely m_I=1/2 is the lower energy level that aligns parallel to the B_0. In most experiments, Zeeman interaction is the dominant interaction that contributes to the signal of NMR spectra because of the magnitude of the strong magnetic field B_0, and all other interactions (see below) can be considered as perturbations of the Zeeman interaction[4,5]. Specifically, the magnetic moment precesses around B_0 with Larmor frequency[5,6] $v_0 = \frac{\gamma}{2\pi} B_0$, which is dependent on the gyromagnetic ratio, an intrinsic property of a nucleus and the strength of the magnetic field. Nuclei that have greater Larmor frequency are preferred for NMR experiments as the larger the Lamour frequencies are, the greater the energy differences $\Delta E = hv_0 = \frac{\mathrm{h}}{2\pi}\gamma \mathrm{B}_0$[4,5], which are correlated to a more detectable energy transition, giving rise to stronger signals. This is because according to Boltzmann distribution[7], the population of different levels can be expressed as $\frac{N_\beta}{N_\alpha} = e^{-\Delta E/kT} = e^{-\mathrm{h}v_0/kT}$, where N_β is the number of spins in higher energy state β, N_α is the number of spins in lower energy state α, h is Planck's constant (6.626 × 10-34 J·s), k is the Boltzmann constant (1.38×10^{-23} JK^{-1}) and T is temperature in Kelvin. Since NMR signals are induced by the transition between different energy levels, the difference of population between energy levels is significant. Based on the Boltzmann distribution, in the presence of external magnetic field B_0, a greater Larmor precession will induce a greater transition from α state to β state ($N_\alpha > N_\beta$), inducing stronger NMR signals.

However, the population difference between these two states is genuinely small, which limits the sensitivity of NMR experiments.

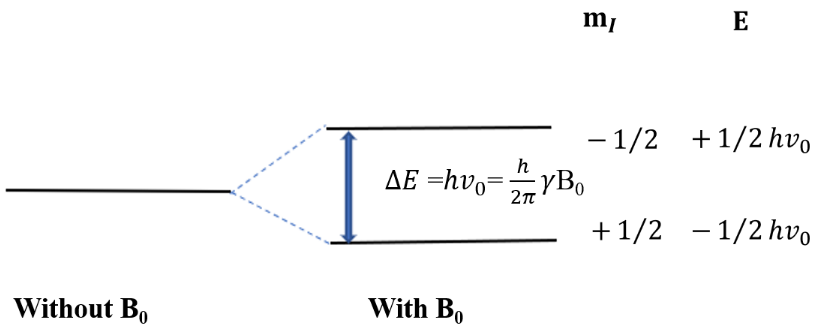

Figure 2-1: Zeeman splitting of a spin-1/2 nucleus such as ^{13}C in B_0.

2.1.2 Radio frequency interaction

In addition to B_0, another oscillating external magnetic field, radio frequency field[4] (B_1), is needed to alter the net magnetization[6] (M_0) by rotating it 90° from z-axis to the x-y plane (Figure 2-2). When the frequency of radio frequency pulse (v_{rf}) is set near the Lamour frequency (v_0), it can induce nuclear spin state transition, resulting in a spin population transition from the low-spin state to the high-spin state. After the 90° pulse, B_1 is switched off and the magnetization will try to go back to thermodynamic equilibrium that precesses at Larmor frequency v_0 in the presence of external magnetic field B_0 via spin-lattice relaxation (T_1) or spin-spin relaxation (T_2). T_1 determines how fast the population equilibrates between the high energy and low energy state by measuring the relaxation time for M_0 to go back to B_0 along z-axis. To illustrate, T_1 determines the length of experimental time since the length of pulse delay is usually $5T_1$ to ensure the spin is back to equilibrium completely before the next scan. T_2, similarly, determines how fast the precession of spin states lose their coherence in x-y plane (Figure 2-3). During this process, a weak induced electric current can be produced in a detecting coil, which is detected as the NMR signal, namely free induced decay (FID). Since FID is in time domain, a Fourier transformation is applied, which will further transform the signal to frequency domain

(Figure 2-4). The interaction between nuclear spin and B_1 is defined as radio frequency interaction.

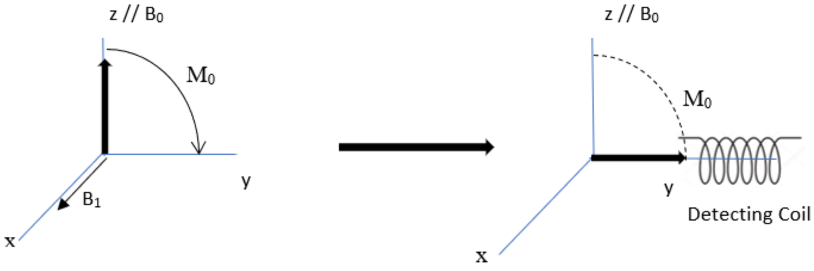

Figure 2-2: Magnetization (M_0) rotated by the radio frequency field B_1.

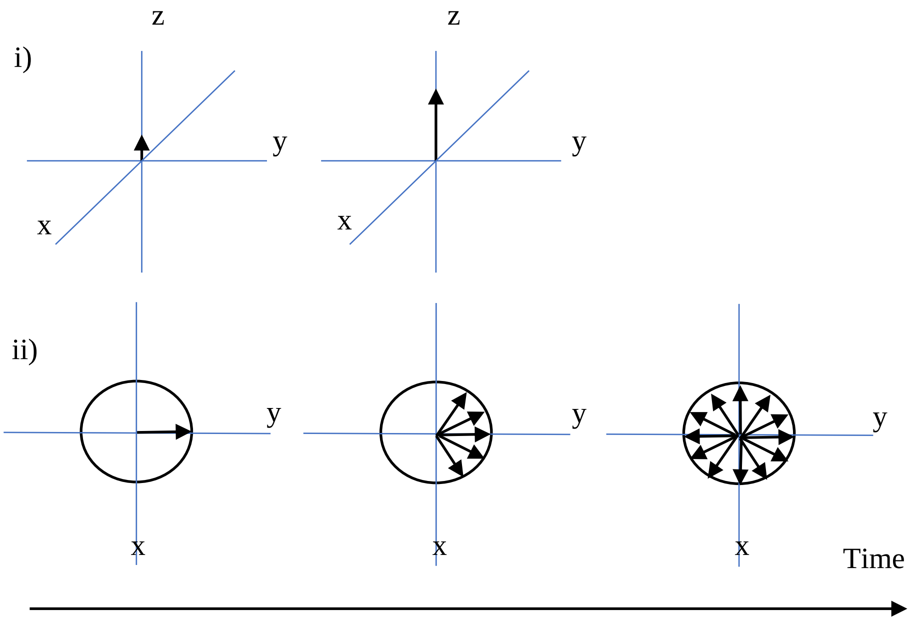

Figure 2-3: i) T_1 relaxation and ii) T_2 relaxation.

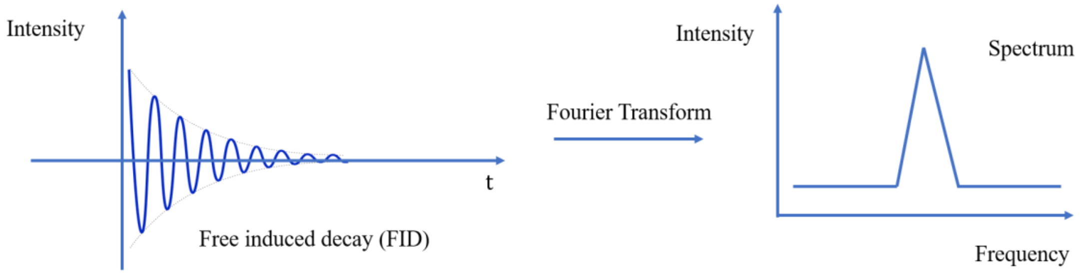

Figure 2-4: Transformation from time to frequency domain.

In addition to Zeeman and radio frequency interactions, a few more internal interactions[4,5] also participate as part of NMR interactions, which can be summarized with the formula $\hat{H}_{NMR} = \hat{H}_Z + \hat{H}_{rf} + \hat{H}_{CS} + \hat{H}_D + \hat{H}_J + \hat{H}_Q$, where Z, rf, CS, D, J, Q represent Zeeman, radio frequency, chemical shielding, dipolar coupling, J-coupling and quadrupolar interactions, correspondingly. Table 2-2 lists the typical NMR nuclear spin interactions with their estimated magnitudes[5].

Table 2-2: Estimated magnitudes of typical NMR nuclear spin interactions. (Reproduced from Ref. 5)

Interaction	**Magnitude (Hz)**
Zeeman	10^7-10^9
Radio Frequency	10^3-10^5
Chemical Shielding	10^3-10^5
Dipolar Coupling	10^3-10^4
J-coupling	1-10^3
Quadrupolar	10^3-10^7

2.1.3 Dipolar interaction

Dipolar interaction exists when two spins denotated as spin I and spin S[4] are in close proximity such as ^{13}C and ^1H in a C-H bond. However, unlike J-coupling in solution NMR, the dipolar interaction is via space, not chemical bonds. Each nucleus with a μ[4] acts as a tiny magnetic bar and yields a local magnetic field that perturbs the other nucleus that either align with or against B$_0$. The strength of the dipolar interaction can be measured by dipolar coupling constant D= $\frac{\mu_0}{4\pi}\frac{\gamma_I\gamma_S}{r^3{}_{IS}}\frac{h}{2\pi}$, where $\mu_0$is the permeability of vacuum, r_{IS} is the inter-spin distance, γ_I, γ_S are the gyromagnetic ratios for spin I and S, correspondingly[4]. The observed precession frequency under the effects of the dipolar interaction can be derived by v= $v_0 \pm \frac{1}{2}D(1 - 3cos^2\alpha\ )$, where v_0 is the nuclear Lamour frequency under B$_0$ and α is the angle in between the inter-spin vector and B$_0$ (Figure 2-5i). Apparently, dipolar interaction is primarily dependent on the gyromagnetic ratio of each spin, the inter-nuclear distance and also the angle α (i.e. the orientation of the internuclear vector in the external magnetic field).

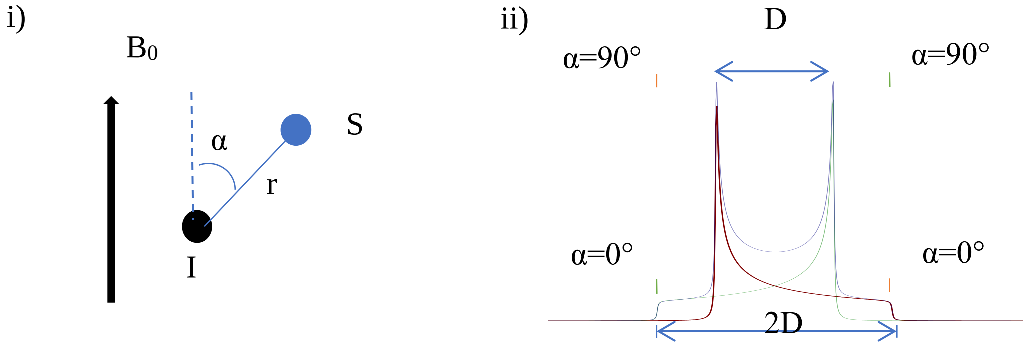

Figure 2-5: i) The schematic demonstration of the principle of magnetic dipolar interaction. ii) A simulated static dipolar coupling NMR spectrum attributed to two heterogeneous nuclei I and S. Here, the maroon and green lines represent the dipole perturbation of nuclei I that either enhance or diminish the magnetic field that nucleus S feels. The blue line is the integrated Pake doublet powder pattern.

Additionally, the typical NMR spectrum of dipolar interaction, namely Pake doublet[8], for a heteronuclear powder sample is shown in Figure 2-5ii. The Pake doublet is composed of two mirrored individual powder patterns, which are attributed to the opposite dipolar perturbations to the Zeeman interaction, featuring two ‘horns’ and two ‘feet’. Specifically, the two ‘horns’ are derived by the S-I vector that is perpendicular to the B$_0$ and the two ‘feet’ are originated from the S-I vector that is parallel to the B$_0$. Moreover, the frequency gap between the two ‘horns’ is equal to D, which is the dipolar coupling constant, whereas that between the two ‘feet’ equals to 2D. Experimentally, dipolar interaction complicates the interpretation of static spectra, making it difficult to analyze. Magic angle spinning (MAS) experiments, thus provide an accessible approach, which is to spin the sample at a defined angle of 54.74°, which could eliminate the interference of dipolar interaction because when α= 54.74°, $1 - 3cos^2\alpha$=0, v= v_0.

2.1.4 J-coupling

J-coupling interaction is a weak interaction that arises through chemical bonds between nuclei that causes the splitting of resonance in NMR spectrum[5]. Due to the line broadening and small magnitude of J-coupling interaction, J-coupling is less often observed in SSNMR compared to that in solution NMR.

2.1.5 Chemical shift interaction

Chemical shielding interaction is induced by electrons that surround a nucleus[4]. In the presence of external magnetic field, B_0 induces additional motions of electrons that circulate around the nucleus, creating a little secondary magnetic field that shields or deshields the nucleus from B_0 that gives rise to precession deviations in frequency when nuclei precess in B_0. The NMR frequency change caused by the shielding interaction is referred to as chemical shielding. $\hat{H}_{\mathrm{CS}}$ can be described by $\hat{H}_{\mathrm{CS}}=-\gamma\hbar\hat{\imath}\sigma B_0$[4], where î is the spin operator and σ is a second-rank chemical shielding tensor[4] that can be described by a 3 x 3 matrix $\sigma = \begin{pmatrix} \sigma_{xx} & \sigma_{xy} & \sigma_{xz} \\ \sigma_{yx} & \sigma_{yy} & \sigma_{yz} \\ \sigma_{zx} & \sigma_{zy} & \sigma_{zz} \end{pmatrix}$.

Because solely the symmetric chemical shielding tensor components compose the appearance of NMR spectra, to make the chemical shift interaction characterizable, three chemical shielding tensor components $(\sigma_{11}, \sigma_{22}, \sigma_{33})$ are defined from the diagonal of symmetrized chemical shielding tensors matrix in principal axis system (PAS)[5], $\sigma^{PAS} = \begin{pmatrix} \sigma_{11} & 0 & 0 \\ 0 & \sigma_{22} & 0 \\ 0 & 0 & \sigma_{33} \end{pmatrix}$. The PAS orients within the molecular framework. The three principle components can be further converted to respective chemical shift (CS) $\delta_{11}, \delta_{22}, \delta_{33}$ by $\delta =$

$\frac{\omega-\omega_{ref}}{\omega_{ref}} \times 10^6 = \frac{\sigma_{ref}-\sigma}{\sigma_{ref}} \approx (\sigma_{ref} - \sigma)$[5], which are more commonly seen in NMR spectra as the CS is B_0 independent and can be experimentally measured. $\sigma_{11}, \sigma_{22}, \sigma_{33}$ align orthogonally and describe the extent of chemical shielding in all three dimensions, where σ_{11} is the least shielded component and σ_{33} is the most shielded component ($\sigma_{11} < \sigma_{22} < \sigma_{33}$). Conversely, the three CS components are ordered in a way that $\delta_{11} > \delta_{22} > \delta_{33}$ since δ_{11} appears at the highest frequency and δ_{33} at the lowest (Figure 2-6). Typically, the three chemical shielding tensors in CO_2 are oriented shown in Figure 2-7i and a simulated ^{13}C SSNMR spectrum of rigid static CO_2 molecule is shown in Figure 2-7ii with $\delta_{11} = \delta_{22}$.

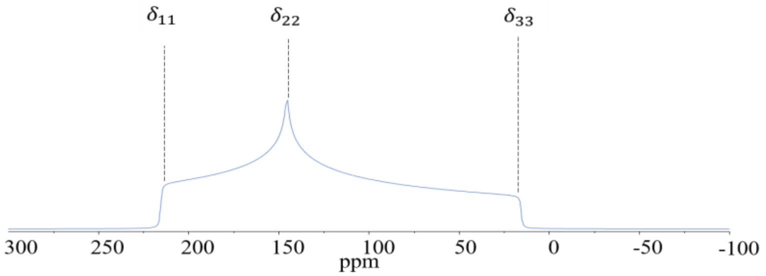

Figure 2-6: A representation of the relative magnitudes of three chemical shift components with $\delta_{11} > \delta_{22} > \delta_{33}$.

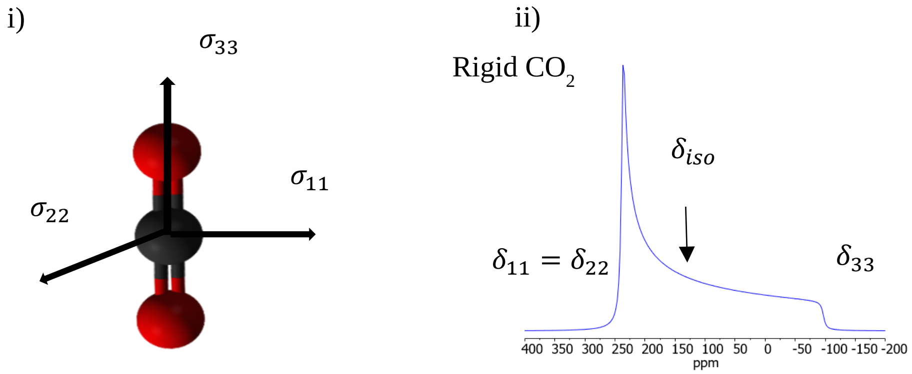

Figure 2-7: i) A representation of the three ^{13}C chemical shielding tensors along three orthogonal directions in CO_2. Atom colors: O-Red, C-Black ii) A simulated ^{13}C SSNMR spectrum of rigid CO_2 molecule. (δ_{iso}=125 ppm, Ω=335 ppm, κ =1)[9].

Furthermore, in the PAS, the chemical shielding frequency shift can be defined as[4] $\nu_{cs}(\theta, \phi) = -\nu_0(\sigma_{11}\sin^2\theta\cos^2\phi + \sigma_{22}\sin^2\theta\sin^2\phi + \sigma_{33}\cos^2\theta)$, where θ, ϕ are polar angles that illustrate the direction of B_0 in the PAS frame as shown in Figure 2-8. When a shielding tensor has axial symmetry ($\sigma_{11}=\sigma_{22}$), the frequency shift can be simplified to[4] $\nu_{cs}(\theta) = -\nu_0 \sigma_{33}\frac{1}{2}(3\cos^2\theta-1)$. Therefore, based on the equation, the chemical shielding is anisotropic, i.e. directionally-dependent and the magnitude depends on the specific orientation of a molecule in the B_0, determined by the various combination of θ and ϕ. In a powdered sample, since every possible orientation of the crystallites with respect to the external magnetic field exists, the observed chemical shielding is distinct for every crystallite that has a unique orientation with respect to the external field, leading to a different frequency. As a result, the observed broad powder pattern corresponds to a distribution of frequency. On the contrary, in solution or gaseous-phase, because molecules tend to undergo fast isotropic (i.e. direction-independent) tumbling motion, the CSA is averaged to its isotropic value, leading to a sharp line.

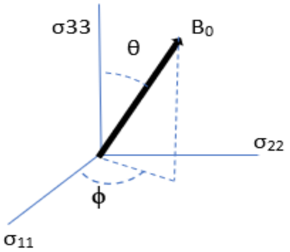

Figure 2-8: The orientation of B_0 in the PAS frame defined by polar angles θ and ϕ.

In addition, based on the chemical shift values, in a chemical shift anisotropy (CSA) powder pattern, the pattern parameters including isotropic chemical shift (δ_{iso}), span (Ω) and skew (κ) of NMR spectra can be derived by $\delta_{iso} = \frac{\delta_{11}+\delta_{22}+\delta_{33}}{3}$, $\Omega = \delta_{11} - \delta_{33}$, $\kappa = \frac{3(\delta_{22}-\delta_{iso})}{\Omega}$, correspondingly[5]. Specifically, δ_{iso} is the isotropic chemical shift, where the positive and negative values correspond to the nucleus that is deshielded and shielded with respect to the reference compound; Ω measures the spectral breadth of the powder pattern in ppm; κ illustrates the asymmetry of the CSA powder pattern that ranges from -1 to 1 and determines where the relative position of the central powder pattern 'horn' is. When κ is equal to either 1 or -1, the chemical shift tensor is regarded as axially symmetric, while the CS tensor is axial asymmetric when κ =0. Broadly speaking, the CS powder pattern is axially symmetric when the nucleus sits at a site with a rotational symmetry ≥ C_3 and axially asymmetric CS powder patterns are seen when the nucleus has C_2 or less rotational symmetry. How the CSA powder patterns vary in respect to the CSA parameters is plotted below (Figure 2-9).

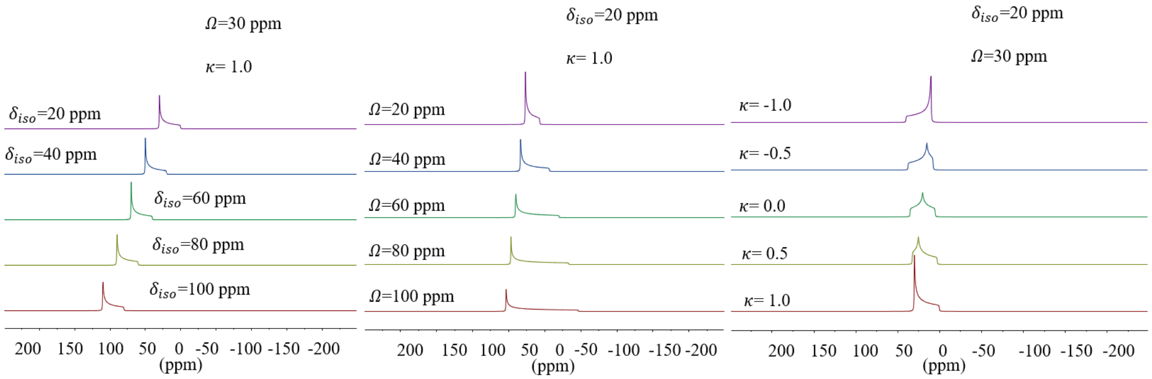

Figure 2-9: Simulated ^{13}C CSA powder patterns to illustrate the effects of isotropic chemical shift δ_{iso}, span Ω, skew κ on spectrum.

2.2 Experimental background of SSNMR

2.2.1 Spin-echo pulse sequence

The pulse sequence used in this thesis for collecting ^{13}C SSNMR spectra of CO_2 adsorbed in MOFs is spin-echo sequence, which allows one to acquire a broad CO_2 powder pattern without lineshapes distortion[10]. As mentioned previously, after the radio frequency field B_1 is turned off, M_0 goes back to the equilibrium that aligns with B_0 and the spin states loss their phase coherence in the x-y plane during T_1 and T_2 relaxation, respectively. During this transverse magnetization process, a weak current could be collected by a detecting coil in the y-axis, which is recorded as the FID signals. Ideally, since the broad signal has a short T_2, the NMR receiver should be turned on immediately after a perfect π/2 (90°) pulse so that the FID can be collected right away without loss of signals. However, in real time, there is a dead time between the end of the π/2 pulse and when the receiver is gated to collect signals to prevent pulse breakthrough and pulse imperfection. Since the broad signals usually decay swiftly, if the current cannot be measured immediately, the signals cannot be collected properly and a large part of the FID will be lost. Furthermore, different frequencies that compose the broad CSA powder pattern lose their phase coherence during the dead time, leading to a distorted NMR lineshape. To overcome these issues, spin-echo (also known as Hahn-echo) can be used to avoid the problems mentioned above. Basically, the spin-echo pulse sequence starts with a $\pi/2$ pulse that rotates the net magnetization M_0 towards the x-y plane by the radio frequency field B_1 along the x-axis, followed by a delay τ. During this time period, spins with different frequencies evolve in the x-y plane. A π (180°) pulse is then applied along the y-axis that rotates the magnetization 180° in respect to the y-axis[4]. At the end of the second delay (τ), an echo is formed. Since at the echo, the dispersed spin magnetization due to the CSA is refocused[4], the observed line shape is free from the distortion (Figure 2-10).

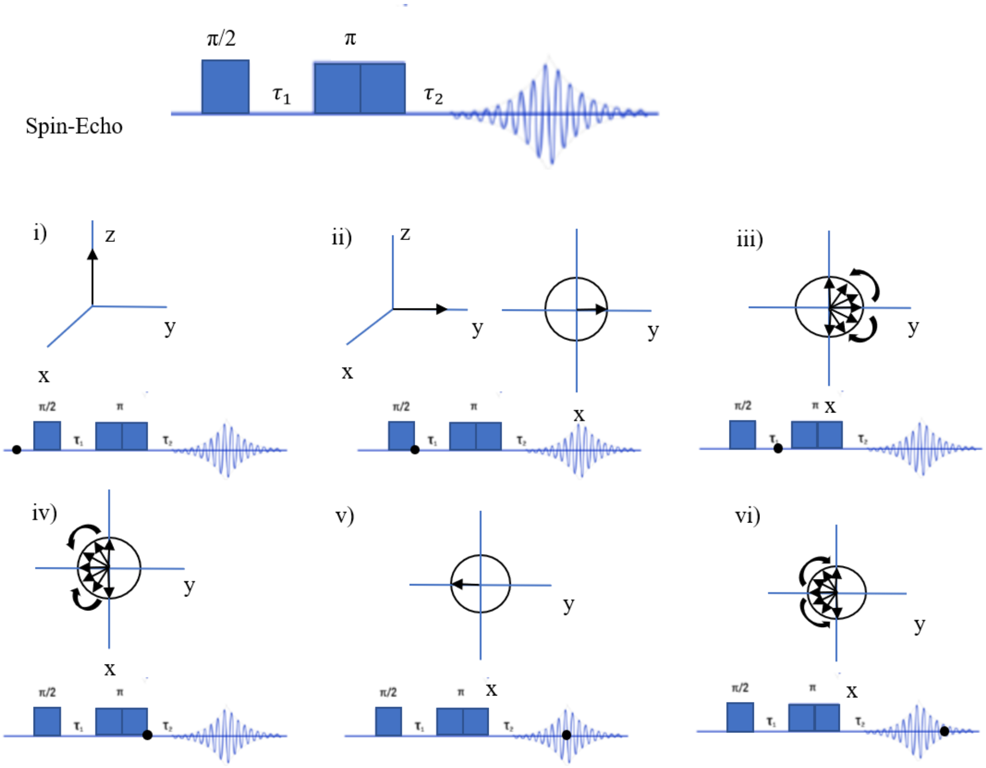

Figure 2-10: Spin-echo pulse sequence, along with the procedures of spin echo magnetization components from i) to vi).

2.3 SSNMR for studying molecular motion in solids

2.3.1 Introduction

Overall, SSNMR is regarded as a well-suited characterization approach to investigate the host-guest interactions, structures and adsorptive properties of MOFs, as well as the dynamics of guest molecules. In SSNMR, all nuclear spin interactions in solid samples are anisotropic (directional dependent) that give rise to broad powder patterns with low signal-to-noise ratio (S/N) rather than sharp resonances that are mostly seen in solution NMR. Since how guest molecules such as CO_2 interact with the framework determines the orientations of CO_2, which affect the local environment of nuclear spins and NMR frequencies, molecular motion changes the orientation of CO_2 in a MOF, affecting the breadth and lineshape of the CO_2 powder pattern[4,11].

2.3.2 ^{13}C static NMR

^{13}C static (non-spinning) SSNMR, was chosen to study molecular motions because ^{13}C is a spin-1/2 nucleus. The lineshape of a ^{13}C powder pattern is highly sensitive to molecular motions due to the dominance of the anisotropic chemical shift interaction. By loading the ^{13}C enriched $^{13}CO_2$ to a MOF, the dynamics of $^{13}CO_2$ can be examined. Variable temperature (VT) SSNMR experiments, particularly, are the most direct method to study the CO_2 dynamics because it reveals how the lineshapes of the CO_2 loaded MOFs change with temperature[12-16].

2.3.3 Processing and simulation software

Two types of spectral simulations are employed: analytical and dynamic simulation. The WSolids software[17] is the analytical simulation that is used to simulate the ^{13}C SSNMR experimental spectra and to extract the apparent ^{13}C NMR parameters δ_{iso}, Ω and κ. It should be noted that when a spectrum has more than one signal, it can be deconvolute and each powder pattern can be simulated to obtain its NMR parameters.

EXPRESS (EXchange Program for RElaxing Spin System)[18], in addition, is the software employed to reveal the dynamic information on specific nuclei to acquire molecular motion types, rates and motional angles etc. The simulation requires the knowledge of the CS parameters and known parameters of the rigid static guest molecules $^{13}CO_2$ (δ_{iso}=125 ppm, Ω=335 ppm, κ =1)[9].

Essentially, the analysis of the experimental spectra can be summarized into the following steps. To begin with, after experimental spectra are acquired, the experimental spectra can be simulated and deconvoluted using WSolids to individual components (if applicable) that overlap one another, which represent different binding sites of the MOFs. Second, the observed NMR parameters (δ_{iso}, Ω and κ) of each individual powder spectrum at each temperature can be extracted by using WSolids software package. Next, the experimental SSNMR spectra of each site at different temperatures can be further simulated using the simulation software EXPRESS to reveal the particular motions of CO_2 including molecular motion types, rates and motional angles along with the NMR parameters of known static CO_2 molecules. In other words, by assuming a motional rate, and certain type of motions that CO_2 can reasonably undergo, EXPRESS can calculate the ^{13}C spectra, which can be compared and matched with experimental spectra. If the simulated and experimental spectra match well, the motions of CO_2 can be revealed. Typical molecules motions of CO_2 include wobbling and hopping, where wobbling refers to a localized rotation around an axis at an adsorption site and hopping refers to discrete jumping between different adsorption sites. For example, when $^{13}CO_2$ undergoes a two-site (C_2) rotation though a rotation angle β_1= 40°, the lineshape is presented in Figure 2-11i and when $^{13}CO_2$ undergoes a three-site (C_3) wobbling rotation through a rotation angle β_2= 40°, the line shape is shown in Figure 2-11ii. Figure 2-11iii represents the spectrum lineshape when CO_2 undergoes combinational motions of C_2 hopping (β) and C_3 wobbling (α) through rotation angles α=β=40°. Notably, by undergoing different types of motions, the simulated ^{13}C powder patterns exhibit distinct lineshapes.

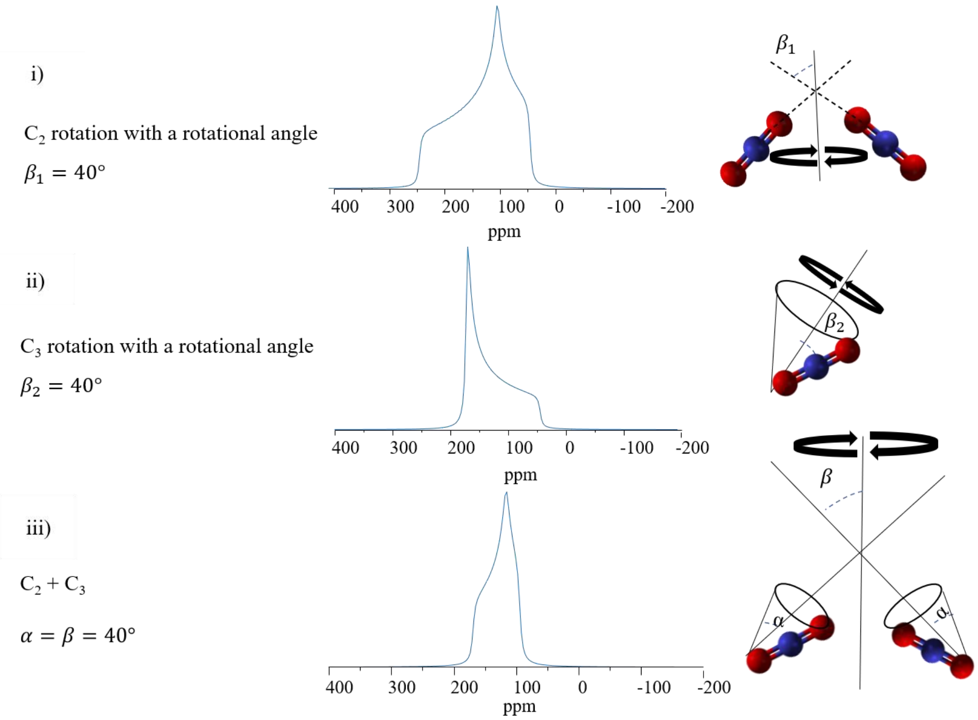

Figure 2-11: The simulated ^{13}C SSNMR spectra of i) $^{13}CO_2$ undergoing a C_2 hopping rotation between two sites through a rotation angle $\beta_1 = 40°$, ii) $^{13}CO_2$ undergoing a C_3 wobbling rotation through a rotation angle $\beta_2 = 40°$, iii) $^{13}CO_2$ undergoing both C_3 and C_2 rotations through rotation angles α and β (α=β=40°), respectively. Atom colors: O-Red, C-Blue. Note: the values of angles are arbitrarily chosen.

Additionally, determining the motional rates or regimes is significant before calculating the simulated ^{13}C spectra as they have tremendous effect on the lineshapes. Basically, whether CO_2 molecules undergo motions in the fast, intermediate or slow-limited regimes all depend on the magnitudes of the exchange rate, k_{ex}, between two sites A and B, which have different isotropic chemical shifts that are in exchange relative to the frequency difference, $\Delta\omega = \omega_A - \omega_B$[19], leading to characteristic lineshapes. The rate of the motion can cause either narrowing or broadening of the powder patterns and the exchange between the two chemical shift environments is considered a temperature-driven process[56] since the mobility of the guest molecules is temperature-dependent.

To begin with, when guest molecules are in the slow exchange regime (at low temperatures, k_{ex} << $\Delta\omega$), guest molecules CO_2 are highly immobile with limited exchange between the two sites. As the exchange rate surges, comparable to the frequency difference ($k_{ex} \approx \Delta\omega$), gas molecules are in the intermediate exchange regime, where the motion of CO_2 is on the order of NMR timescale and the lines are more broadened. Next, when the exchange rate further increases (at higher temperature), greater than the NMR frequency separation (k_{ex} >> $\Delta\omega$), CO_2 molecules are in the fast motion regime and are exceedingly dynamic. In the fast motional regime, the peaks narrow again that only a single resonance is observed on the NMR spectrum and the motion of CO_2 is said to be faster than the NMR time scale[20]. Typically, when the exchange rate is > 10^7 Hz, the motion of CO_2 is considered in the fast-limit regime and the lineshapes of NMR spectra do not change with surpassing exchange rate; When the rate is < 10^3 Hz, the motion is in the slow-limit regime; When the rate is $10^3 < k_{ex} < 10^7$ Hz, the motion is considered in the intermediate regime and the lineshapes of NMR spectra usually vary from one to another at different exchange rate. To illustrate these points, the ^{13}C SSNMR spectra of $^{13}CO_2$ undergoing C_2 hopping (α=50°) at different exchange rate are simulated using EXPRESS (Figure 2-12). As the exchange rate increases, the motion of CO_2 shifts from slow to intermediate and fast-limited regime, exhibiting different lineshapes.

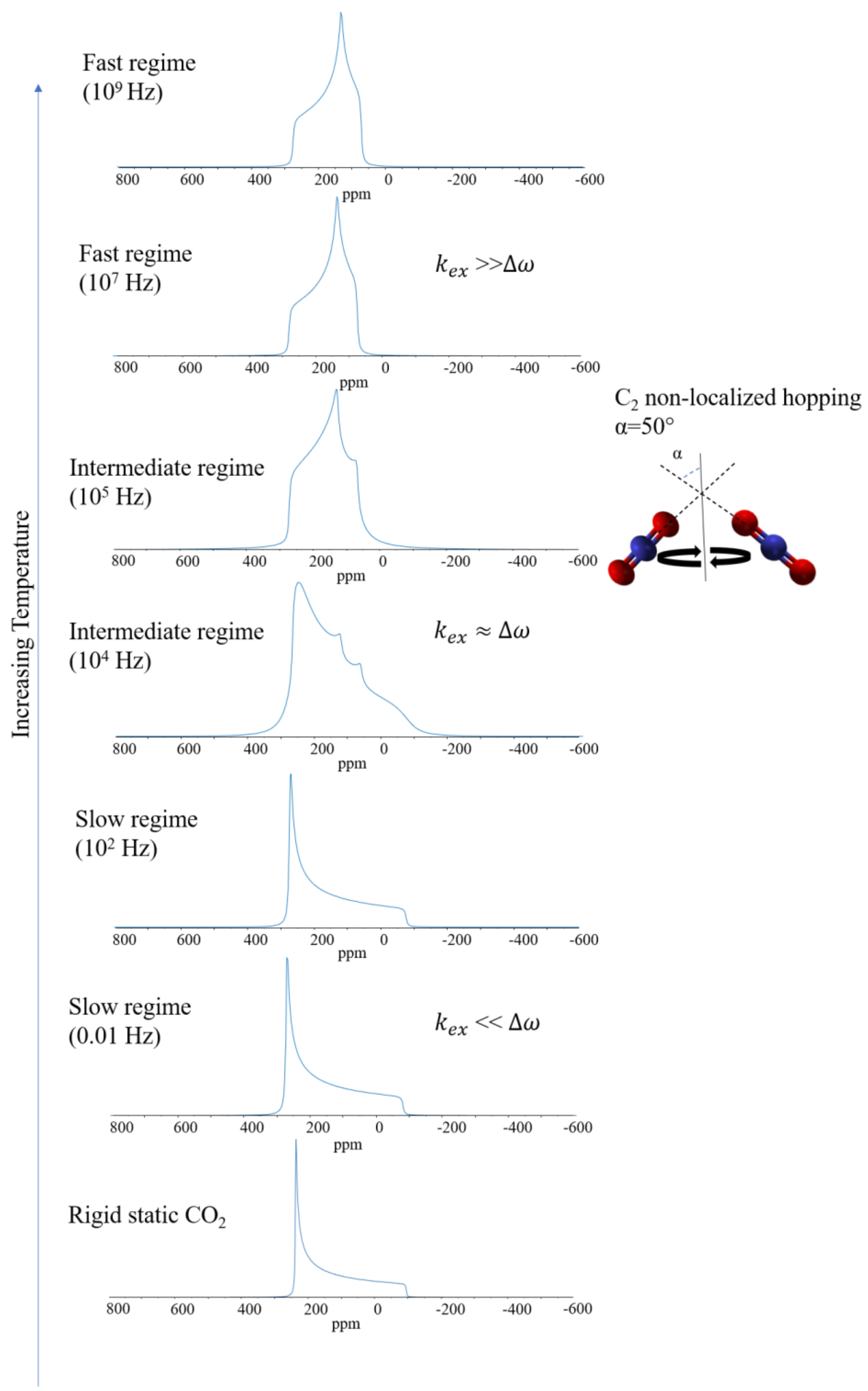

Figure 2-12: The simulated ^{13}C SSNMR spectra of $^{13}CO_2$ undergoing C_2 rotations through rotation angles α =50° at various exchange rates. When the exchange rate is < 10^3 Hz, $^{13}CO_2$ molecules are in the slow-limited regime and there is no exchange between sites of

different chemical shift environments. As the exchange rate increases that the rate of exchange is $10^3 < k_{ex} < 10^7$ Hz, $^{13}CO_2$ are in the intermediate regime with broadened lines. As the rate further increases, the lines narrow again and only a single resonance is observed on the NMR spectrum as $^{13}CO_2$ are in the fast-limited regime with exchange rate $>10^7$ Hz. The ^{13}C SSNMR spectrum of rigid static CO_2 is simulated at the bottom.

2.4 Bibliography

1. Sutrisno, A.; Huang, Y. Solid-State NMR: A Powerful Tool for Characterization of Metal–Organic Frameworks. *Solid State Nuclear Magnetic Resonance* **2013**, *49-50*, 1–11.
2. Hoffmann, H. C.; Debowski, M.; Müller, P.; Paasch, S.; Senkovska, I.; Kaskel, S.; Brunner, E., Solid-state NMR Spectroscopy of Metal–Organic Framework Compounds (MOFs). *Materials* **2012,** *5* (12), 2537-2572.
3. Levitt, M. H., *Spin Dynamics*. Second ed., John Wiley & Sons West Sussex, **2008**.
4. Duer, M. J., *Solid-State NMR Spectroscopy: Principles and Applications*. Blackwell Science, Oxford, **2002**.
5. MacKenzie, K.; Smith, M. E., *Multinuclear Solid-State Nuclear Magnetic Resonance of Inorganic Materials*. Pergamon: Oxford New York, **2002**.
6. Keeler, J., *Understanding NMR Spectroscopy*. Second ed., John Wiley & Sons, West Sussex, **2010**
7. Nelson, J. H., *Nuclear Magnetic Resonance Spectroscopy*. Pearson Education, Upper Saddle River, **2003**.
8. Pake, G. E., Nuclear Resonance Absorption in Hydrated Crystals: Fine Structure of the Proton Line. *The Journal of Chemical Physics* **1948,** *16* (4), 327-336.
9. Beeler, A. J.; Orendt, A. M.; Grant, D. M.; Cutts, P. W.; Michl, J.; Zilm, K. W.; Downing, J. W.; Facelli, J. C.; Schindler, M. S.; Kutzelnigg, W., Low-Temperature Carbon-13 Magnetic Resonance in Solids. 3. Linear and Pseudolinear Molecules. *Journal of the American Chemical Society* **1984,** *106* (25), 7672-7676.
10. Hahn, E. L. Spin Echoes. *Physical Review* **1950**, *80* (4), 580–594.
11. Tycko, R., *Nuclear Magnetic Resonance Probes of Molecular Dynamics*. Kluwer Academic, Netherlands, **1994**.
12. Kong, X.; O'Dell, L. A.; Terskikh, V.; Ye, E.; Wang, R.; Wu, G. Variable-Temperature ^{17}O NMR Studies Allow Quantitative Evaluation of Molecular Dynamics in Organic Solids. *Journal of the American Chemical Society* **2012**, *134* (35), 14609–14617.

13. Lucier, B. E.; Chen, S.; Huang, Y. Characterization of Metal–Organic Frameworks: Unlocking the Potential of Solid-State NMR. *Accounts of Chemical Research* **2017**, *51* (2), 319–330.
14. Wang, W. D.; Lucier, B. E.; Terskikh, V. V.; Wang, W.; Huang, Y. Wobbling and Hopping: Studying Dynamics of CO_2 Adsorbed in Metal–Organic Frameworks via 17O Solid-State NMR. *The Journal of Physical Chemistry Letters* **2014**, *5* (19), 3360–3365.
15. Zhang, Y.; Lucier, B. E.; Huang, Y. Deducing CO_2 Motion, Adsorption Locations and Binding Strengths in a Flexible Metal–Organic Framework without Open Metal Sites. *Physical Chemistry Chemical Physics* **2016**, *18* (12), 8327–8341.
16. Wong, Y. T.; Martins, V.; Lucier, B. E.; Huang, Y. Solid-State NMR Spectroscopy: A Powerful Technique to Directly Study Small Gas Molecules Adsorbed in Metal–Organic Frameworks. *Chemistry – A European Journal* **2018**, *25* (8), 1848–1853.
17. Eichele K.; Wasylishen R. E., *WSolids1* University of Tübingen, Tübingen, Germany, **2009**.
18. Vold, R. L.; Hoatson, G. L., Effects of Jump Dynamics on Solid State Nuclear Magnetic Resonance Line Shapes and Spin Relaxation Times. *Journal of Magnetic Resonance* **2009,** *198* (1),57-72.
19. Waudby, C. A.; Ouvry, M.; Davis, B.; Christodoulou, J. Two-Dimensional NMR Lineshape Analysis of Single, Multiple, Zero and Double Quantum Correlation Experiments. *Journal of Biomolecular NMR* **2020**, *74* (1), 95–109.
20. Witherspoon, V. J.; Xu, J.; Reimer, J. A. Solid-State NMR Investigations of Carbon Dioxide Gas in Metal–Organic Frameworks: Insights into Molecular Motion and Adsorptive Behavior. *Chemical Reviews* **2018**, *118* (20), 10033–10048.

Chapter 3

3 Investigating the dynamics and adsorption of $^{13}CO_2$ in UTSA-74 at different loading levels using VT ^{13}C static SSNMR

3.1 Experimental section

3.1.1 MOF synthesis

All chemicals were purchased from Sigma-Aldrich and were used without further purification. UTSA-74 was synthesized using the solvothermal method reported in the literature[1]. $Zn(CH_3COO)_2 \cdot 2H_2O$ (1g, 4.50 mmol), 2,5-dihydroxy-1,4-benzenedicarboxylic acid (H_4DOBDC, 0.5g, 2.50 mmol), and dimethyl sulfoxide (DMSO, 50 ml) were mixed into a 100 ml Teflon-lined stainless steel autoclave and placed in a pre-heated conventional oven at 110 °C for 72 hours. The resulting products were then cooled to room temperature, filtered, and collected under vacuum filtration and dried at 80℃ for 8 hours, after which yellow crystalline powders were obtained, which were regarded as “as-made” (as) UTSA-74.

3.1.2 Sample activation

To load $^{13}CO_2$ guest molecules into UTSA-74, all residual solvent molecules and unreacted chemicals have to be removed from the pores of UTSA-74(as) upon activation. UTSA-74(as) was firstly washed five times with DMSO at room temperature to rinse off the unreacted H_4DOBDC ligands and zinc acetate salts. After that, UTSA-74 was soaked and washed repeatedly with anhydrous ethanol at 80 °C overnight for seven days to remove the DMSO solvent molecules out the pores.

To activate UTSA-74, a Schlenk line was used. Firstly, approximately 150mg of UTSA-74 samples were grounded up to fine powders and were placed into the bottom of a homemade L-shaped glass tube with 5mm in diameter (to fit the 5mm SSNMR coil). Next, a small layer of glass wool was added on top of the powder sample to secure the MOF samples in place. Thirdly, the L-shaped glass tube was attached to the Schlenk line. The Schlenk line was then connected to a vacuum pump and a pressure gauge, which was used to monitor the pressure that should be no greater than 1 mbar under vacuum conditions.

Specifically, all MOFs were heated at 473 K under dynamic vacuum ($\leq$ 1mbar) for 8 hours to remove residual ethanol molecules in the UTSA-74 channels, giving rise to “activated” (ac) UTSA-74.

3.1.3 Gas adsorption

^{13}C isotopically labeled $^{13}CO_2$ (Sigma-Aldrich, 99% ^{13}C isotope enriched) was used in this study as the guest molecules because of ^{13}C’s low natural abundance (0.96%). Generally, the gas adsorption process was carried out after the activation process. To begin with, a known amount of pressurized CO_2 gas was released to the Schlenk line that occupied a total volume of 82.7 cm^3. Next, designated amount of CO_2 was loaded into the L-shaped glass tube, and the bottom part of L-shaped glass tube was immersed into liquid nitrogen to condense CO_2 inside the sample. Moreover, a torch was applied to flame-seal off the L-shaped glass tube so that the CO_2-loaded samples can be separated from the Schlenk line. Based on the amount of CO_2 loaded and the amount of UTSA-74 sample placed into the L-shaped glass tube, the gas loading amount in the MOF can be expressed by the molar ratio between CO_2 guest molecules and the metal Zn. In this thesis, a total of four samples with ascending loading levels (i.e. 0.30, 0.54, 0.90 and 1.48 CO_2/ Zn2) were prepared and characterized by SSNMR. Given the SBU of UTSA-74, the maximum CO_2 loading level for UTSA-74 (ac) is 2 CO_2/ Zn2 since each Zn2 can possibly bind to 2 CO_2 molecules in the axial positions after activation.

3.1.4 Powder X-ray diffraction (pXRD)

pXRD is an analytical technique used to measure the diffraction patterns of crystalline materials and confirm the identity of prepared crystalline materials (e.g. MOFs) by comparing the diffractograms with those reported in the literature. All pXRD diffractograms were acquired using a Rigaku diffractometer operating with Co Kα radiation (λ = 1.7902 Å). Diffractograms were collected at 2θ values ranging from 5 to 45 degrees with an increment of 0.02° at a scanning rate of 10°/ min. The experimental and simulated pXRD powder patterns are depicted in Figure S3-1 in the appendix. The experimental diffractograms are in good agreement with the simulated diffractogram of literature reported UTSA-74[2].

3.1.5 Thermogravimetric analysis (TGA)

TGA is a technique used to measure the thermal stability of MOFs and confirm the removal of solvent from the framework after sample activation. The samples were heated under dry N_2 flow using a Mettler Toledo TGA/SDTA851e instrument from 25 °C to 800 °C at a constant heating rate of 10 °C/min. The resulting TGA curves are depicted in Figure S3-2. In the activated UTSA-74, a weight loss of 3% between 133 °C to 184 °C is observed, indicating that the majority of solvent has been removed after the activation, while a small amount of solvent in the UTSA-74 framework remains.

3.1.6 ^{13}C static SSNMR

SSNMR experiments were conducted by using a Varian Infinity Plus 400 spectrometer that operated with an Oxford 9.4 T magnet and a Varian/Chemagnetics 5mm HX static probe. A Varian VT temperature control unit was used to adjust the temperature from 133 K to 373 K. Experimental temperature readings were measured ± 2 K and calibrated by ^{207}Pb chemical shift of solid $Pb(NO_3)_2$[3]. When a new temperature was researched, there was 20 minutes elapsed time in order to achieve thermal equilibrium of the system. The chemical shift of ^{13}C spectra was referenced to the methylene carbon of ethanol, which is at 56.83 ppm from tetramethylsilane (TMS).

All SSNMR spectra were acquired using the spin-echo pulse sequence[4]. Experimental parameters including the ^{13}C 90° pulse length, optimized pulse delay, two delay times τ_1 and τ_2 and number of scans are listed in Table 3-1.

Table 3-1: The experimental parameters setup of VT ^{13}C static SSNMR carried out in UTSA-74 at different $^{13}CO_2$ loading amount.

	0.30 CO_2/ Zn2	0.54 CO_2/ Zn2	0.90 CO_2/ Zn2	1.48 CO_2/ Zn2
90° pulse length (pw90)	2.9 μs	3.8 μs	3.8 μs	2.5 μs
pulse delay (pd)	4s	3s	4s	4s
τ_1	40μs	40μs	40μs	40μs
τ_2	20μs	20μs	20μs	20μs
Acquisition numbers (scans)	173K-293K 1120	173K-373K 1024-1888	133K-333K 1120	173K-313K 1600
	Except 153K 2016	Except 293K 15552		Except 293K 2048

3.2 Results and discussion

3.2.1 VT ^{13}C static SSNMR experiments on low $^{13}CO_2$-loaded UTSA-74

The experimental and simulated ^{13}C NMR spectra of the UTSA-74 at a loading level of 0.54 $^{13}CO_2$/ Zn2 within the temperature range from 173 K to 373 K are exhibited in Figure 3-1i, 3-1ii. Overall, CO_2 is mobile at all temperatures because the span of every powder pattern is much smaller than that of solid CO_2 (Ω=335 ppm)[5] and the interaction between CO_2 and the UTSA-74 framework is temperature-dependent since the powder patterns exhibit different lineshapes as the experimental temperatures increase from 173 K to 373 K. Next, in the entire range of temperature, CO_2 was found to be adsorbed in the MOF as there was no narrow sharp resonance with isotropic chemical shift at 125 ppm, which corresponds to free gaseous CO_2. This is because the chemical shift anisotropy (CSA) related lineshape broadening is averaged out when free gaseous CO_2 rapidly tumbles isotropically inside the pore, leading to a single sharp resonance. At higher temperatures, the powder patterns tend to be narrower, indicating that CO_2 is more mobile. On the contrary, when temperature is reduced to 173 K, the powder pattern is much broader, corresponding to highly immobile CO_2 due to the loss of thermal energy, which illustrates a tighter and stronger interaction between CO_2 and UTSA-74 framework.

Importantly, the simulated spectra by WSolids reveal that the broad and asymmetric NMR powder pattern of the UTSA-74 (0.54 $^{13}CO_2$/ Zn2) is explicitly composed of two separate powder patterns, which indicates that there are two CO_2 adsorption sites in the

MOF (Figure 3-1iii, 3-1iv). The apparent CS parameters (δ_{iso}, Ω, κ) for both sites were determined from simulations and are given in Table 3-2. $^{13}CO_2$ adsorbed at site 1 exhibits a change in spectral breadth with temperature, i.e. the span (Ω) steadily increases from 65 ppm to 185 ppm as the temperature decreases from 373 K to 173 K, while the skew (κ) and the isotropic chemical shift (δ_{iso}) change little as temperature decreases. The greater values of span at lower temperatures indicate that CO_2 is adsorbed to the framework more tightly with less mobility. Conversely, the variation of span and skew at site 2 is not significant as both parameters remain consistent with only slight fluctuations as temperature goes down from 373 K to 173 K. The isotropic chemical shift values of site 2 also remain unchanged. Notably, the site occupancies do not change significantly with temperature and are approximately 60% and 40% for site 1 and 2, respectively. As mentioned earlier, the spans of both sites are much smaller than that of rigid CO_2 ($\Omega = 335$ ppm, $\kappa = 1$)[5] at the lowest temperature reached (173 K), suggesting that the CO_2 molecules still undergo anisotropic motion(s) even at 173 K.

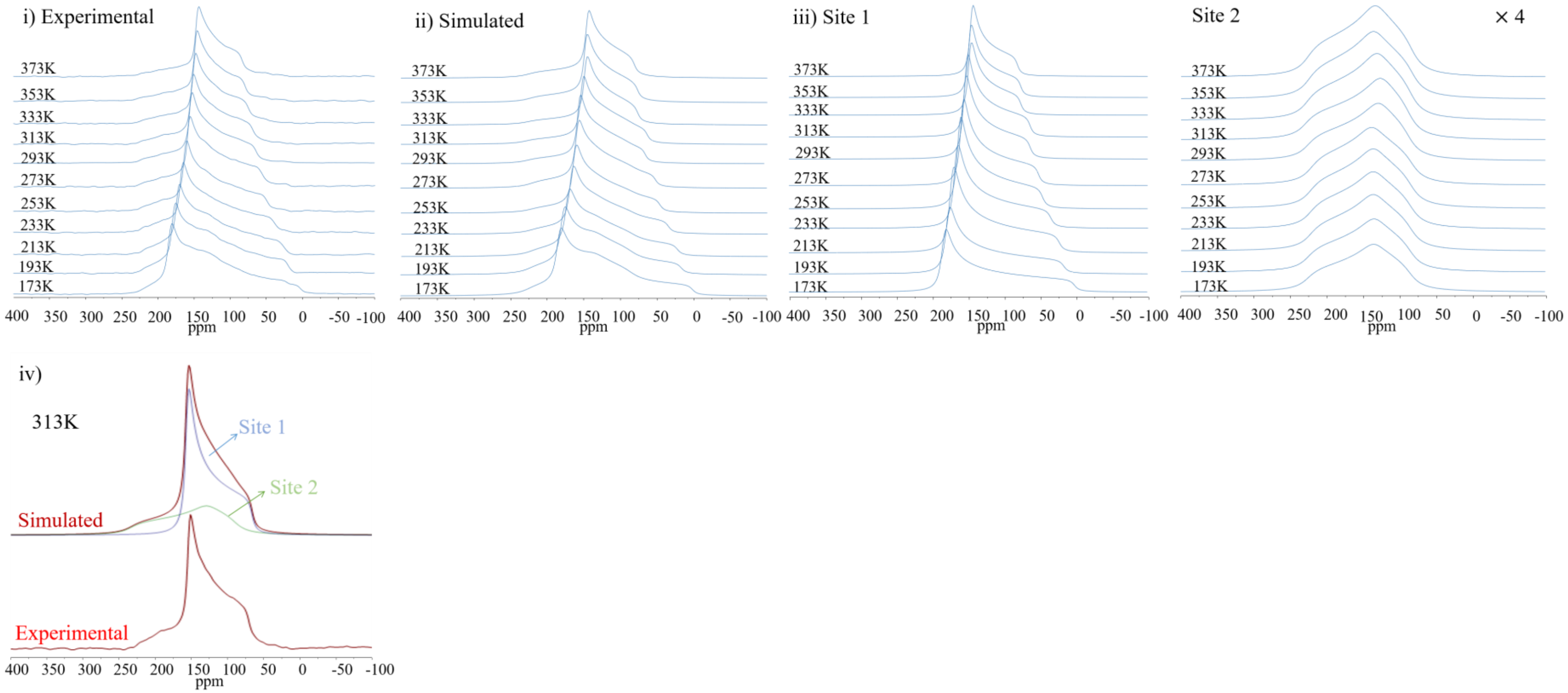

Figure 3-1: i) Experimental. ii) Simulated VT ^{13}C static NMR spectra of the UTSA-74 at a loading level of 0.54 $^{13}CO_2$/ Zn2 at temperatures ranging from 173 K to 373 K. iii) Simulated spectra of site 1 and site 2 from 173 K to 373 K using WSolids. The intensity of the site 2 is scaled up by a factor of 4. iv) Experimental and simulated spectra of the UTSA-74 (0.54 $^{13}CO_2$/ Zn2) at 313 K and the deconvoluted components of site 1 (blue) and site 2 (green).

Table 3-2: The apparent ^{13}C chemical shift parameters of CO_2 adsorbed at site 1 and site 2 in the UTSA-74 (0.54 $^{13}CO_2$/ Zn2) from 173 to 373 K.

	Site 1				Site 2			
Temperature(K)	δ_{iso}(ppm)	Ω	κ	Site 1%	δ_{iso}(ppm)	Ω	κ	Site 2%
373K	123.5(5)	65(1)	0.95(5)	57%	147(1)	142(2)	-0.30(5)	43%
353K	123.5(5)	71(1)	0.95(4)	56%	147(1)	142(1)	-0.20(5)	44%
333K	123.5(5)	72(2)	0.95(3)	57%	147(2)	150(3)	-0.20(5)	43%
313K	122.5(5)	90(1)	0.95(2)	59%	147(1)	142(2)	-0.20(6)	41%
293K	124.0(5)	94(2)	0.95(5)	56%	147(1)	150(2)	-0.10(5)	44%
273K	122.5(5)	108(1)	0.95(2)	59%	147(1)	150(2)	-0.10(2)	41%
253K	123.5(5)	118(1)	0.95(2)	59%	147(1)	160(1)	0.10(5)	41%
233K	123.0(5)	134(1)	0.95(3)	61%	147(1)	160(2)	0.10(5)	39%
213K	122.5(5)	152(1)	0.95(3)	63%	147(1)	140(2)	-0.20(8)	37%
193K	124.0(5)	164(1)	0.95(1)	63%	147(1)	130(3)	-0.30(7)	37%
173K	122.5(5)	185(2)	0.95(1)	63%	147(1)	140(2)	-0.25(5)	37%

The possible motional modes of the CO_2 at site 1 and site 2 can be determined through dynamical simulation using the EXPRESS software package. The EXPRESS-simulated ^{13}C SSNMR powder patterns for both sites were obtained under the fast motion regime, as the motional rate was set to be at least 10^7 Hz. For site 1, the simulated powder patterns reveal that CO_2 molecules undergo two types of motions: a localized wobbling motion modeled by a six-fold (C_6) rotation and a non-localized three-fold (C_3) hopping motion (Figure 3-2i). Both motions are defined by an angle between the long molecular axis of CO_2 and the rotational axis. For site 1, α and β are the angles defining C_6 and C_3 rotation, respectively. Their values at different temperatures are listed in Table 3-3. As the temperature increases, the value of α increases concomitantly from 20.0° at 173 K to 43.5° at 373 K. Such change is reasonable since at lower temperatures, the interaction between CO_2 molecules and UTSA-74 framework is tighter, thus CO_2 tends to wobble around the adsorption sites with smaller angles, leading to less mobility. The angle β remains consistent and does not vary with temperature.

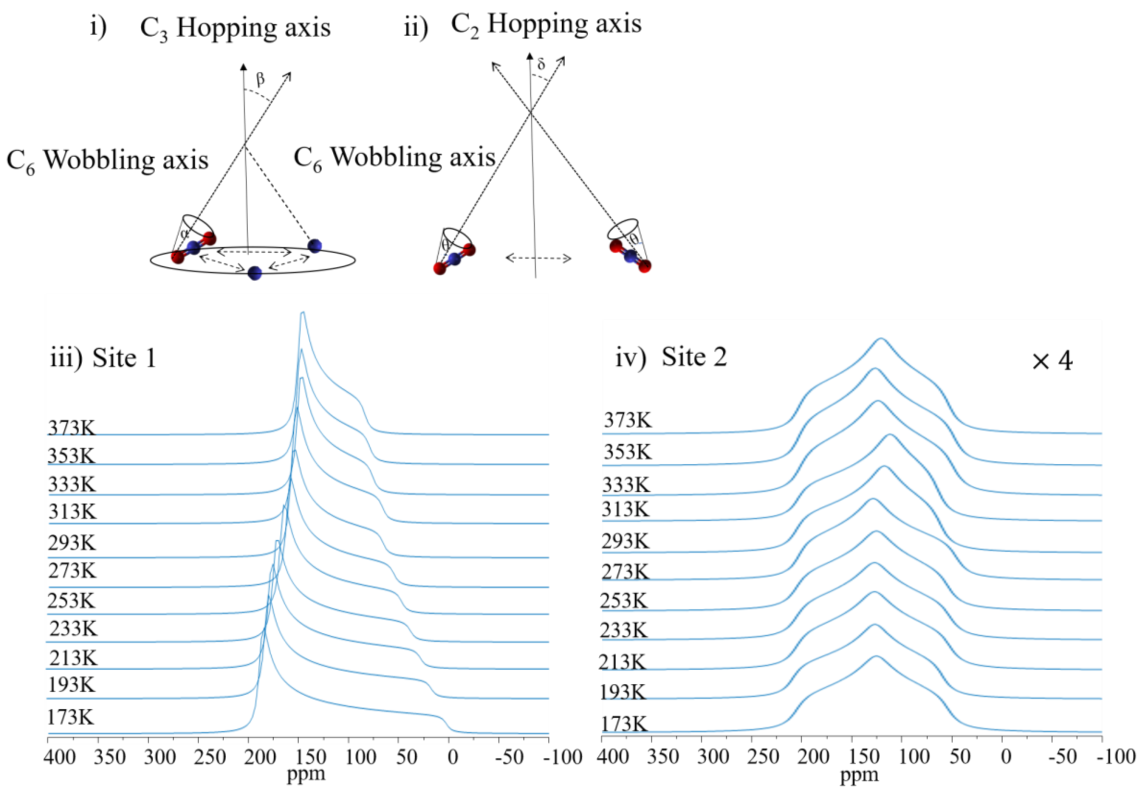

Figure 3-2: In the UTSA-74 at a loading level of 0.54 $^{13}CO_2$/ Zn2: i) CO_2 undergoes a localized C_6 wobbling with a rotation angle α and a non-localized C_3 hopping with a rotation angle β at site 1. ii) CO_2 undergoes a localized six-fold wobbling (C_6, θ) and a non-localized two-fold hopping (C_2, δ) at site 2. Atom colors: O-Red, C-Blue. The simulated spectra of Site 1 iii) and Site 2 iv) are plotted from 173 K to 373 K using EXPRESS. The intensity of the site 2 is scaled up by a factor of 4.

Table 3-3: The rotation angles of α, β for site 1 and θ, δ for site 2 in the UTSA-74 (0.54 $^{13}CO_2$/ Zn2) from 173 to 373 K.

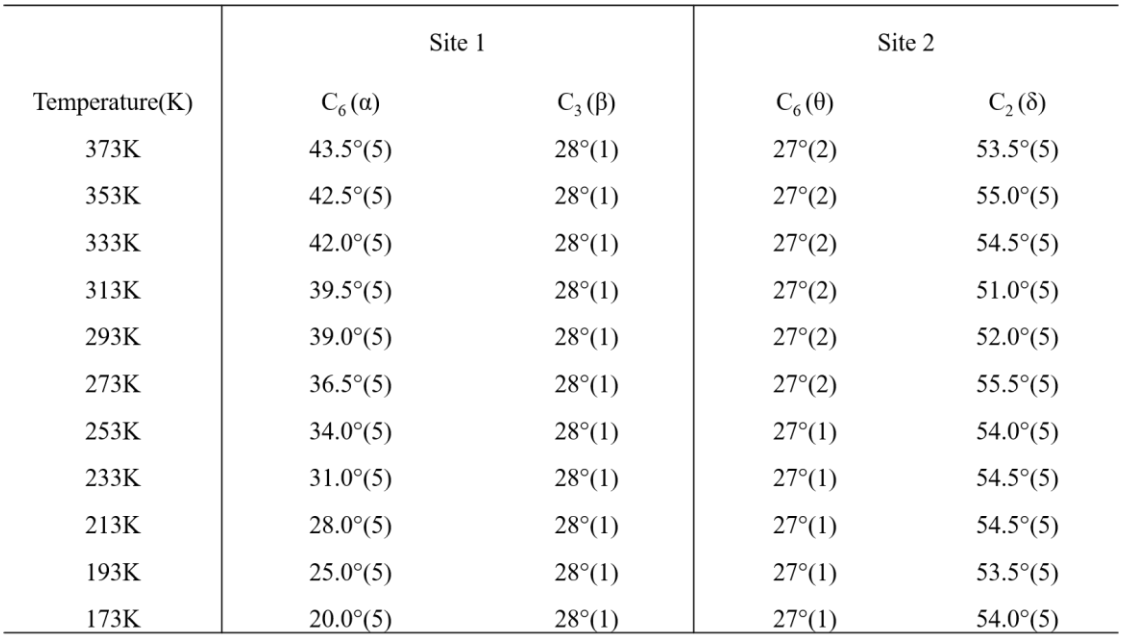

	Site 1		Site 2	
Temperature(K)	C_6 (α)	C_3 (β)	C_6 (θ)	C_2 (δ)
373K	43.5°(5)	28°(1)	27°(2)	53.5°(5)
353K	42.5°(5)	28°(1)	27°(2)	55.0°(5)
333K	42.0°(5)	28°(1)	27°(2)	54.5°(5)
313K	39.5°(5)	28°(1)	27°(2)	51.0°(5)
293K	39.0°(5)	28°(1)	27°(2)	52.0°(5)
273K	36.5°(5)	28°(1)	27°(2)	55.5°(5)
253K	34.0°(5)	28°(1)	27°(1)	54.0°(5)
233K	31.0°(5)	28°(1)	27°(1)	54.5°(5)
213K	28.0°(5)	28°(1)	27°(1)	54.5°(5)
193K	25.0°(5)	28°(1)	27°(1)	53.5°(5)
173K	20.0°(5)	28°(1)	27°(1)	54.0°(5)

The distinct motions of CO_2 at site 1 are most likely determined by the coordination environment of Zn atoms in UTSA-74. Recall that each SBU of UTSA-74 encloses two types of Zn^{2+}: Zn1 is tetrahedrally coordinated with no available binding sites. Zn2 is in an octahedral geometry with two axial positions occupied by the solvent molecules, i.e. H_2O (Figure 3-3i). Upon activation, the two H_2O molecules are removed, creating two accessible binding sites for CO_2 adsorption (Figure 3-3ii). Specifically, when guest molecules e.g. CO_2 molecules are loaded into the activated UTSA-74, they are able to bind to Zn2 from both ends with equal possibilities. Depending on the loading, the CO_2 can occupy either a single or both axial positions. Here, a loading level of 0.54 CO_2/ Zn2 is reached when a total amount of 56 mbar of $^{13}CO_2$ was loaded into the 170 mg of UTSA-74a at room temperature, which is considered as a low CO_2 loading level (Figure 3-3ii). In this instance, we propose that CO_2 could possibly undergo a localized C_6 wobbling through an angle α between the longitudinal axis of CO_2 and the wobbling axis around the Zn2 adsorption site. At the same time, it also experiences a non-localized C_3 hopping among three Zn2 sites located on the channel cross-section (Figure 3-3iii). The hopping angle β is the angle between CO_2 wobbling axis and an axis particular to the channel cross-section. The combinational C_6+C_3 motions of CO_2 at site 1 are illustrated in Figure 3-3iii. Remarkably, similar types of motion have been observed in MOF-74, the isomer of UTSA-

74. According to the study of Wang et al.[6] and Lin et al.[7], the motion of $^{13}CO_2$ in MOF-74 can be modeled by a localized C_6 wobbling as well as a non-localized C_6 hopping between open metal sites in the channel. The distinction between the motion of hopping is predominantly determined by the difference in the number of OMS on the channel cross-section: In UTSA-74, $^{13}CO_2$ can only jump among three OMS in the channel, whereas all six OMS are accessible in MOF-74-Zn. In addition, based on the experimental spectra presented by Wang et al[6], the span values of all powder patterns in MOF-74 are smaller than that of UTSA-74 and there is no gaseous mobile $^{13}CO_2$ observed in UTSA-74. As a result,$^{13}CO_2$ molecules are less mobile in UTSA-74 and the adsorptive interaction between $^{13}CO_2$ and Zn2 is stronger.

Furthermore, the dynamical simulation of powder spectra for site 2 reveals that CO_2 experiences a combinational six-fold (C_6) wobbling plus a non-localized two-fold (C_2) hopping with rotation angles θ and δ, respectively ($C_6 + C_2$) (Figure 3-2ii). As seen in Table 3-3, both rotation angles θ (27°) and δ (53°$\pm$ 2°) are independent of temperature changes. Herein, the presence of $C_6 + C_2$ motion of CO_2 at site 2 is likely due to the low $^{13}CO_2$ loading amount. According to what Luo et al.[2] suggested, when the loading of CO_2 is low, each CO_2 molecule preferably binds to two neighboring accessible metal sites simultaneously to minimize coordination unsaturation. Given the low CO_2 loading amount (0.54 CO_2/ Zn2), it is reasonable that each CO_2 not only undergoes a localized C_6 wobbling around the Zn2 adsorption site but also hops between two neighboring Zn2 simultaneously (Figure 3-3iv). Figure 3-4 further provides a close view of the connection between each $^{13}CO_2$ and two adjacent Zn2 adsorption sites when only a small amount of $^{13}CO_2$ is introduced to the UTSA-74 framework. Notably, the influence of temperature on CO_2 motions at site 2 seems relatively insignificant as the motions of C_6 wobbling (θ) and C_2 hopping (δ) do not vary much with temperature.

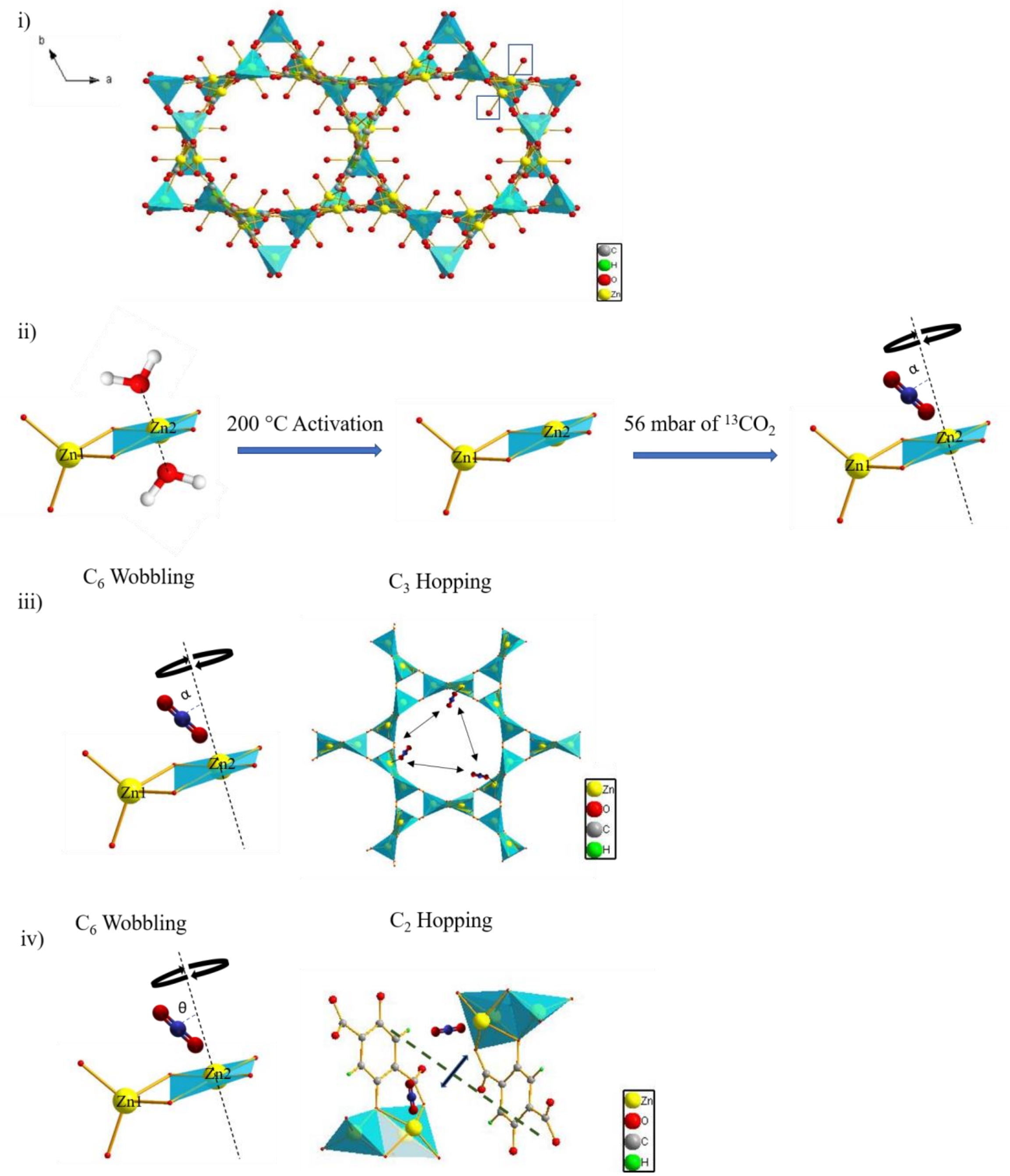

Figure 3-3: i) Solvent molecules H_2O (circled) bind to the Zn2 adsorption sites from both ends, pointing inward and outward. Atom colors: Zn-Yellow, O-Red, C-Grey, H are omitted for simplification. ii) Procedures of $^{13}CO_2$ adsorption in the UTSA-74 at a loading level of 0.54 $^{13}CO_2$/ Zn2. Firstly, each Zn2 adsorption site is occupied by 2 H_2O molecules before samples activation. After H_2O molecules are removed upon activation, two

accessible binding sites are created for $^{13}CO_2$ adsorption. Next, 56 mbar of $^{13}CO_2$ was loaded to UTSA-74a, which occupy one of the axial positions on Zn2. Atom colors: Zn-Yellow, O-Red, C-Blue, H-White. iii) At adsorption site 1, CO_2 undergoes a localized C_6 wobbling through an angle α between the longitudinal axis of CO_2 and the wobbling axis around the Zn2 adsorption site. Simultaneously, CO_2 also experiences a non-localized C_3 hopping among three Zn2 sites located on the channel cross-section. iv) At adsorption site 2: CO_2 undergoes a localized C_6 wobbling (θ) around the Zn2 adsorption site and a non-localized C_2 hopping (δ) between two adjacent Zn2 at the same time. Atom colors: Zn-Yellow, O-Red, C-Grey, H-Green, C from $^{13}CO_2$ are highlighted in blue.

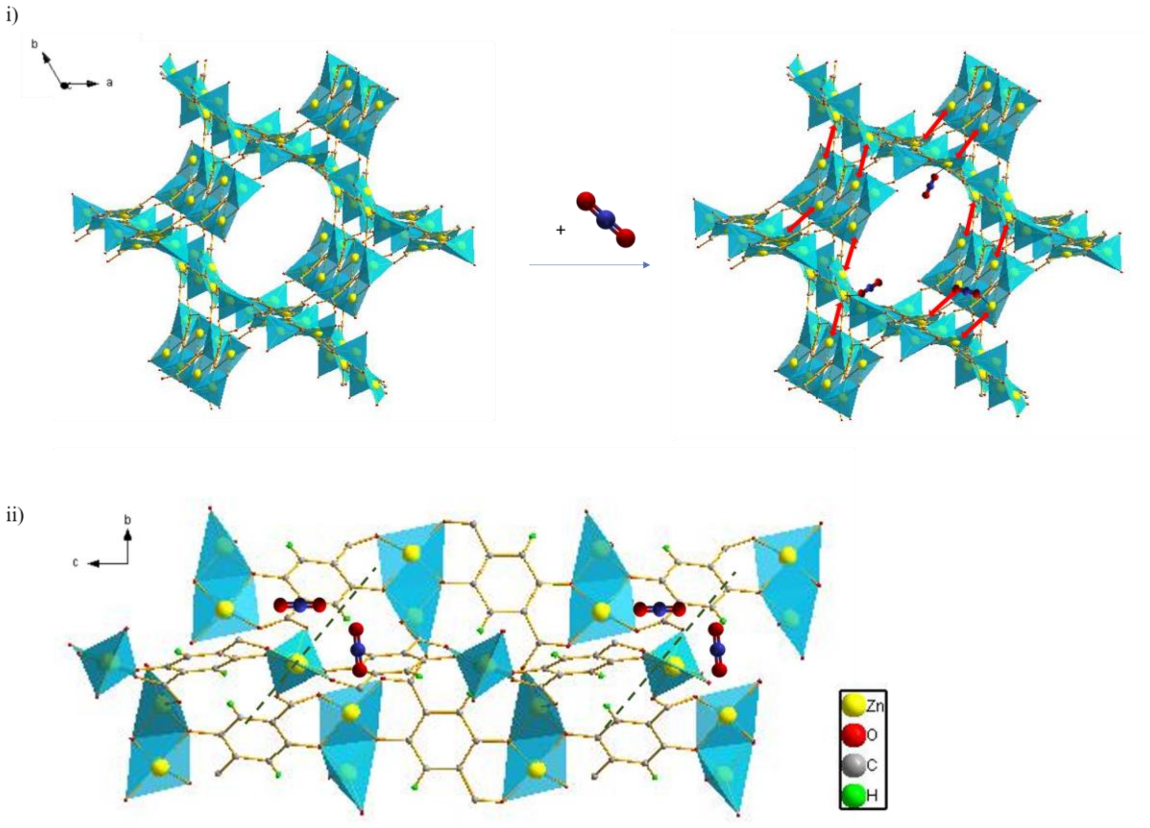

Figure 3-4: i) The structure of empty UTSA-74a (left) and the structure of UTSA-74 loaded with CO_2 (right). In this diagram, how $^{13}CO_2$ molecules undergo the 3-site (C_3) hopping among three non-adjacent Zn2 adsorption sites on the channel cross-section as well as the 2-site (C_2) hopping between two neighboring Zn2 adsorption sites are illustrated. The motion of C_2 hopping is shown by red double arrows. ii) A close view of $^{13}CO_2$ non-

localized C_2 hopping motion. Atom colors: Zn-Yellow, O-Red, C-Grey, H-Green, C from $^{13}CO_2$ are highlighted in blue.

It is interesting to note that for site 2, the span, skew and intensity do not change significantly with temperature, which is contradictory to common knowledge that gas molecules usually have greater degree of mobility at high temperature with narrower lineshape and vice versa. Thus, in this circumstance, we propose that $^{13}CO_2$ is adsorbed exceedingly tightly to the adsorption site 2, which surpasses typical physical adsorption, more resembled to chemisorption. This is due to the formation of carbonate species when CO_2 molecules are adsorbed to MOFs or other porous materials via chemisorption. For example, in the Low-silica X (LSX) zeolites, when CO_2 molecules are tightly adsorbed to K^+ or Na^+ cations in LSX zeolites through chemisorption, carbonate species are formed, which strongly interact with the cations and exhibit very limited mobility[8,9]. In other words, when CO_2 is stably chemisorbed, the lineshapes of ^{13}C powder pattern present minimal changes with temperature. In the present case, the isotropic chemical shift of site 2 (ca. 145ppm) is between the values of physiosorbed CO_2 (ca. 125 ppm[5]), and the carbonate species (ca. 170 ppm[10]). Thus, we tentatively suggest that CO_2 at site 2 strongly interacts with unsaturated Zn2 open metal site. The strength of the interaction is stronger than that of the normal physisorption, resulting in consistent values of rotation angle θ (27°) and δ (53° ± 2°) from 373 K to 173 K. It is worth noting SSNMR is unable to determine the binding energy of between $^{13}CO_2$ and adsorption site 2, but the value of binding energy can be calculated by dispersion-corrected density functional theory (DFT-D). Based on the calculation from Luo et. al, the binding energy is approximately 33.4 kJ/mol[2].

To look into whether the dynamics and motional modes of $^{13}CO_2$ in the UTSA-74 framework would be different when the loading amount is lower, a sum of 23 mbar of $^{13}CO_2$ was loaded into the 125 mg of UTSA-74a samples at room temperature, which gives rise to UTSA-74 with a loading level of 0.30 $^{13}CO_2$/ Zn2. The experimental and simulated ^{13}C NMR spectra of the UTSA-74 (0.30 $^{13}CO_2$/ Zn2) from 153 K to 313 K are displayed in Figure 3-5i, 3-5ii. Similar to the UTSA-74 (0.54 $^{13}CO_2$/ Zn2), there is no unadsorbed

$^{13}CO_2$ in the UTSA-74 (0.30 $^{13}CO_2$/ Zn2) at all temperatures and the interaction between $^{13}CO_2$ and the UTSA-74 framework is temperature-dependent.

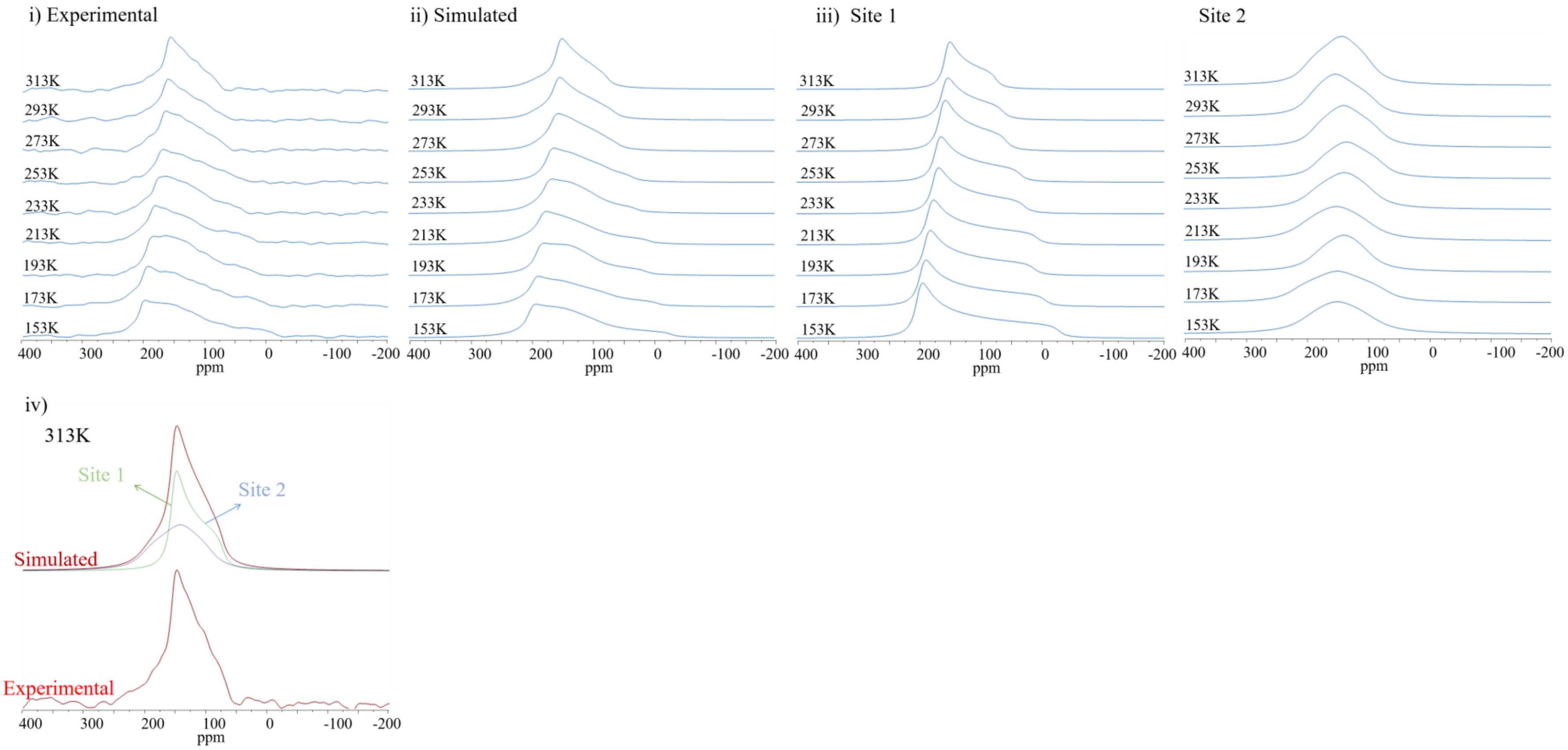

Figure 3-5: i) Experimental. ii) Simulated VT ^{13}C static NMR spectra of the UTSA-74 at a loading level of 0.30 $^{13}CO_2$/ Zn2 at temperatures ranging from 153 K to 313 K. iii) Simulated spectra of site 1 and site 2 from 153 K to 313 K using WSolids. iv) Experimental and simulated spectra of the UTSA-74 (0.30 $^{13}CO_2$/ Zn2) at 313 K and the deconvoluted components of site 1 (green) and site 2 (blue).

Based on analytically simulated VT ^{13}C static NMR spectra from WSolids, there are also two CO_2 adsorption sites in the MOF, as displayed in Figure 3-5iii, 3-5iv. The apparent CS parameters (δ_{iso}, Ω, κ) of $^{13}CO_2$ at each site display a trend analogous to that for the UTSA-74 (0.54 $^{13}CO_2$/ Zn2): At site 1, the span (Ω) steadily expands from 80 ppm to 228 ppm as the temperature decreases from 313 K to 153 K, while the values of skew (κ) stays unchanged (κ=1) as temperature decreases, which correspond to an axially symmetric CS tensor. At site 2, the span and skew remain consistent with slight fluctuations as temperature decreases from 313 K to 153 K (Table 3-4). For this loading, the site occupancies of site 1 and site 2 are approximately equivalent, which each takes up 50%.

Table 3-4: The apparent ^{13}C chemical shift parameters of CO_2 adsorbed at site 1 and site 2 in the UTSA-74 (0.30 $^{13}CO_2$/ Zn2) from 153 to 313 K.

	Site 1				Site 2			
Temperature(K)	iso(ppm)	Ω	κ	Site 1%	iso(ppm)	Ω	κ	Site 2%
313K	126.0(8)	80(3)	1.00(6)	55%	145(2)	110(5)	-0.10(8)	45%
293K	125.0(6)	95(3)	1.00(7)	54%	145(3)	110(4)	0.20(8)	46%
273K	126.0(3)	105(2)	1.00(8)	41%	135(1)	110(4)	0.10(6)	59%
253K	123.0(6)	135(2)	1.00(7)	53%	130(1)	110(4)	0.10(6)	47%
233K	123.5(8)	145(3)	1.00(7)	39%	140(1)	105(5)	-0.10(6)	61%
213K	122.0(8)	175(5)	1.00(7)	43%	150(1)	115(5)	0.00(4)	57%
193K	127.0(5)	175(3)	1.00(7)	49%	140(1)	90(5)	-0.10(8)	51%
173K	126.0(8)	200(3)	1.00(6)	46%	146(2)	150(5)	0.05(5)	54%
153K	122.0(9)	228(3)	1.00(4)	49%	146(1)	110(5)	0.10(8)	51%

The EXPRESS-simulated ^{13}C SSNMR powder patterns further confirm that CO_2 molecules are dynamic, undergoing 1) a localized six-fold (C_6, α) wobbling and a non-localized three-fold (C_3, β) hopping at site 1 as presented in Figure 3-6i; and 2) a localized six-fold (C_6, θ) wobbling and a non-localized two-fold (C_2, δ) hopping at site 2 (Figure 3-6ii) at a motional rate $\geq 10^7$ Hz. The motional angles of α, β for site 1 and θ, δ for site 2 are listed in Table 3-5. Akin to the UTSA-74 (0.54 CO_2/ Zn2), as temperature increases, the value of α increases concomitantly with its smallest value 3.0° at 153 K, and maximum value 40.5° at 313 K, while *β* remains identical (28°) at different temperatures. For site 2, both rotation angles θ and *δ* are consistent with little fluctuation as temperature changes.

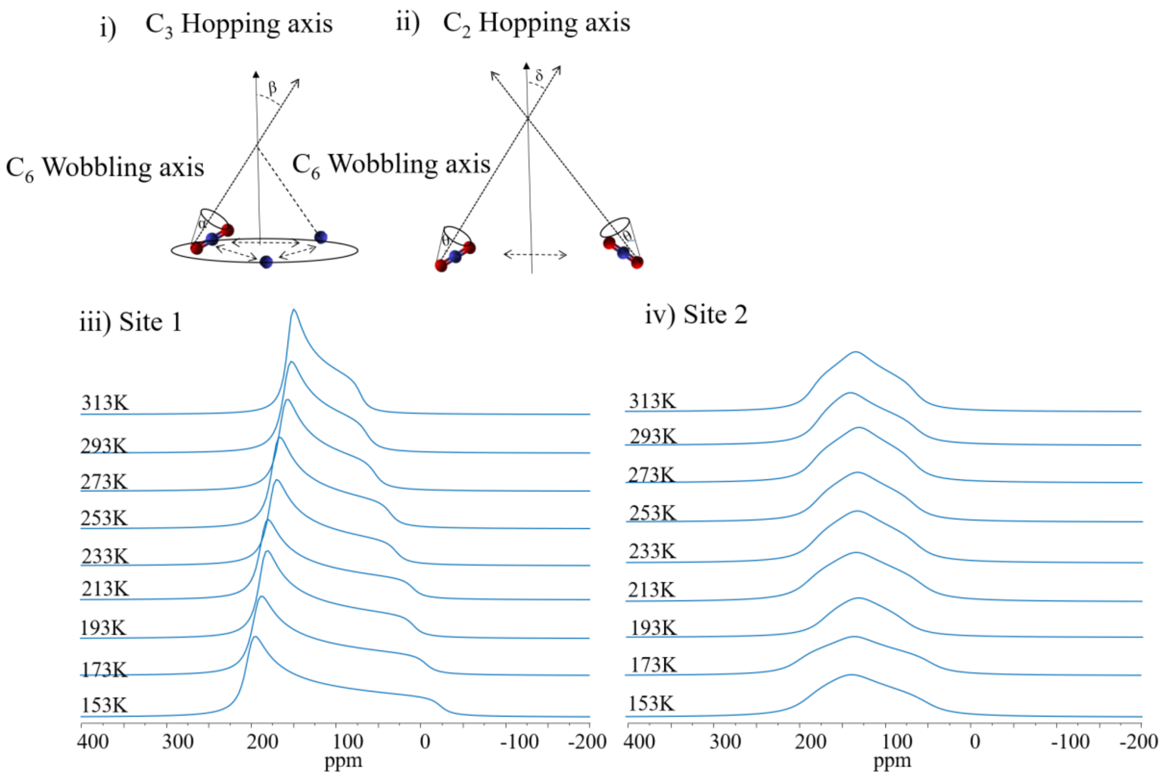

Figure 3-6: In the UTSA-74 at a loading level of 0.30 $^{13}CO_2$/ Zn2: i) CO_2 undergoes a localized C_6 wobbling with a rotation angle α and a non-localized C_3 hopping with a rotation angle β at site 1. ii) CO_2 undergoes a localized six-fold wobbling (C_6, θ) and a non-localized two-fold hopping (C_2, δ) at site 2. Atom colors: O-Red, C-Blue. The simulated spectra of Site 1 iii) and site 2 iv) are plotted from 153 K to 313 K using EXPRESS.

Table 3-5: The rotation angles of α, β for site 1 and θ, δ for site 2 in the UTSA-74 (0.30 $^{13}CO_2$/ Zn2) from 153 to 313 K.

	Site 1		Site 2	
Temperature(K)	C_6 (α)	C_3 (β)	C_6 (θ)	C_2 (δ)
313K	40.5°(5)	28°(1)	35°(1)	33°(1)
293K	38.5°(5)	28°(1)	37°(1)	30°(1)
273K	36.0°(5)	28°(1)	35°(1)	34°(1)
253K	31.0°(5)	28°(1)	36°(1)	33°(1)
233K	29.0°(5)	28°(1)	35°(1)	33°(1)
213K	22.5°(5)	28°(1)	33°(1)	33°(1)
193K	22.0°(5)	28°(1)	39°(1)	33°(1)
173K	16.0°(5)	28°(1)	29°(1)	33°(1)
153K	3.0°(5)	28°(1)	33°(1)	31°(1)

Noticeably, the motional modes of the UTSA-74 at 0.30 CO_2/ Zn2 and 0.54 CO_2/ Zn2 loading level are the same, which suggests that our proposal towards $^{13}CO_2$ motions at low loading level is reasonable. By looking at the CS parameters and rotation angles at site 1, the span values of the 0.30 $^{13}CO_2$/ Zn2 are greater than that of the 0.54 $^{13}CO_2$/ Zn2, along with smaller C_6 wobbling angles at temperatures < 253 K. This indicates that the mobility of $^{13}CO_2$ is lower at the UTSA-74 (0.30 $^{13}CO_2$/ Zn2). In addition, the steady values of span, $^{13}CO_2$ rotation angles at the entire temperature range and the similar values of δ_{iso} at the 0.30 $^{13}CO_2$/ Zn2 site 2 further suggest that our proposal at the 0.54 $^{13}CO_2$/ Zn2 site 2 is reasonable: $^{13}CO_2$ undergoes fairly strong interaction with Zn2 that the motion of $^{13}CO_2$ is limited.

However, how would the motion of $^{13}CO_2$ change if the loading level is higher? Luo et al.[2] have suggested that the adsorption configuration may shift to one $^{13}CO_2$ per metal at a high $^{13}CO_2$ loading but lack of detailed experimental explanation. To explicitly understand the motions of CO_2 within the UTSA-74 framework, VT ^{13}C static SSNMR experiments were carried out at UTSA-74 samples in both moderate and high CO_2 loading levels.

3.2.2 VT ^{13}C static SSNMR experiments on moderate and high $^{13}CO_2$-loaded UTSA-74

In principle, each Zn2 can, at maximum capacity, bind to two $^{13}CO_2$ molecules after activation. Thus, a moderate loading level is reached when half of the Zn2 adsorption sites are occupied by $^{13}CO_2$ molecules, which is approximately 1 $^{13}CO_2$/ Zn2. In other words, at a moderate loading level, each Zn2 adsorption site, on average, adsorbs about one $^{13}CO_2$. A high loading level corresponds to the loading where every Zn2 is occupied by at least one $^{13}CO_2$ and a significant number of Zn2 are coordinated to two $^{13}CO_2$ molecules. In this instance, the motions of $^{13}CO_2$ might be different from what has been observed at the low loading levels. Therefore, the behavior of $^{13}CO_2$ at the high and moderate loading levels was investigated. The results allow us to understand the relation between $^{13}CO_2$ motions and loading levels more comprehensively.

A total amount of 100 mbar $^{13}CO_2$ was loaded into 110 mg of UTSA-74a, giving rise to UTSA-74 with a loading level of 1.48 $^{13}CO_2$/ Zn2. The experimental and simulated ^{13}C NMR spectra from 153 K to 313 K are displayed in Figure 3-7i, 3-7ii. Again, there is no free gaseous $^{13}CO_2$ observed and the lineshapes of the broad and asymmetrical powder patterns are temperature-dependent.

Analytically simulated VT ^{13}C static NMR spectra indicate that there are two CO_2 adsorption sites in the MOF at this high loading, as displayed in Figure 3-7iii, 3-7iv. For site 1, the observed ^{13}C CS parameters of adsorbed $^{13}CO_2$ change with temperature. Specifically, the value of span (Ω) steadily increases from 50 ppm to 150 ppm as the temperature decreases from 313 K to 153 K, while skew (κ) changes from 0.40 to 0.60 with little fluctuations (Table 3-6). In addition, δ_{iso} values at site 1 mainly lie between 121-125 ppm, which suggest that $^{13}CO_2$ is bound to adsorption site 1 via physisorption. This is in good alignment with the results presented at the low loading levels. Comparatively, the Ω and κ values in the UTSA-74 (1.48 $^{13}CO_2$/ Zn2) site 1 are smaller than those in the 0.54 and 0.30 $^{13}CO_2$/ Zn2, indicating that the mobility of $^{13}CO_2$ at the UTSA-74 (1.48 $^{13}CO_2$/ Zn2) is higher. However, for site 2, the values of span, skew and intensity do not change dramatically with temperature, which is similar to the situation found for site 2 at the low loadings. Besides, the values of δ_{iso} are more deshielded than 125 ppm[5], which imply that

$^{13}CO_2$ is adsorbed more tightly to the adsorption site 2, surpassing the binding strength of typical physisorption.

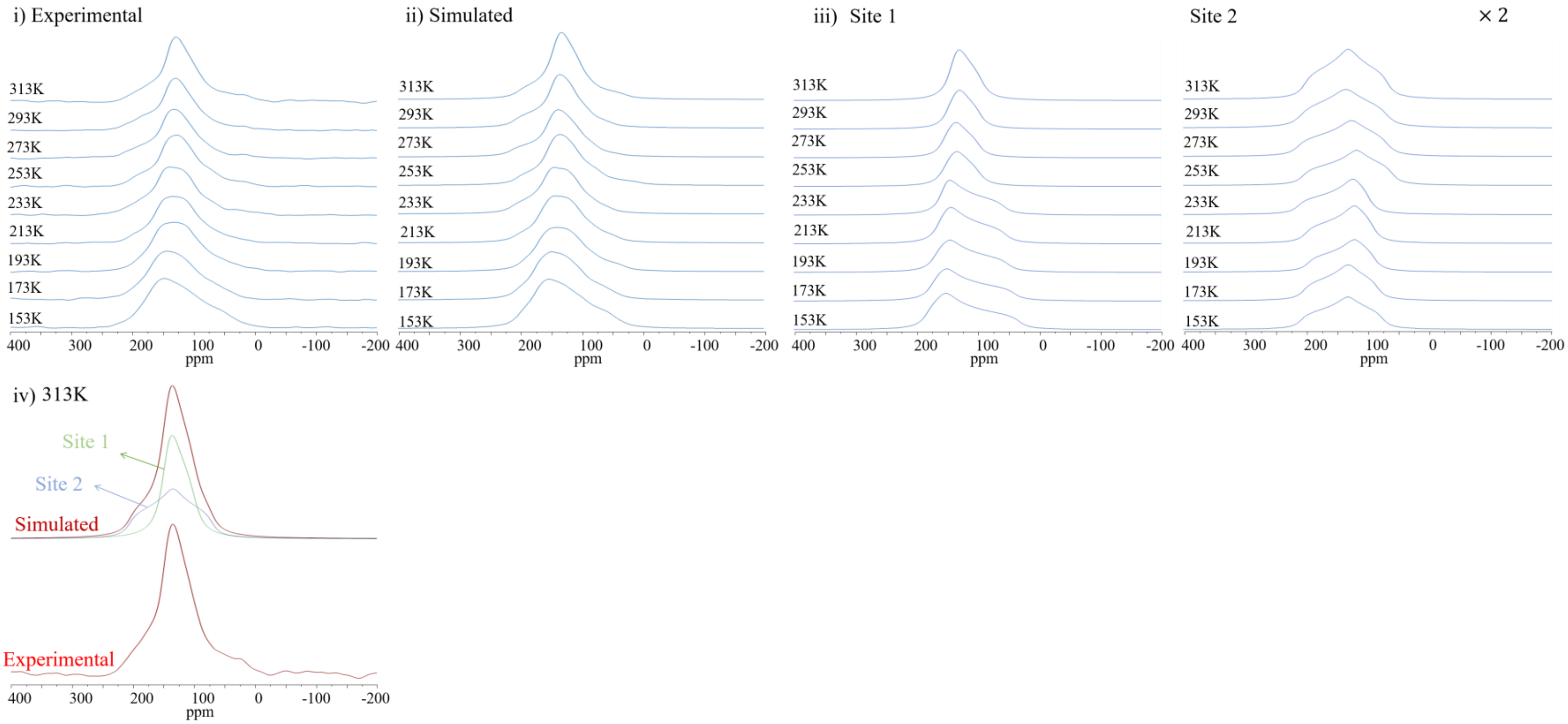

Figure 3-7: i) Experimental. ii) Simulated VT ^{13}C static NMR spectra of the UTSA-74 at a loading level of 1.48 $^{13}CO_2$/ Zn2 at temperatures ranging from 153 K to 313 K. iii) Simulated spectra of site 1 and site 2 from 153 K to 313 K using WSolids. The intensity of the site 2 is scaled up by a factor of 2. iv) Experimental and simulated spectra of the UTSA-74 (1.48 $^{13}CO_2$/ Zn2) at 313 K and the deconvoluted components of site 1 (green) and site 2 (blue).

Table 3-6: The apparent ^{13}C chemical shift parameters of $^{13}CO_2$ adsorbed at site 1 and site 2 in the UTSA-74 (1.48 $^{13}CO_2$/ Zn2) from 153 to 313 K.

	Site 1				Site 2			
Temperature(K)	iso(ppm)	Ω	κ	Site 1%	iso(ppm)	Ω	κ	Site 2%
313K	123(1)	50(3)	0.40(9)	54%	131(1)	135(3)	-0.15(9)	46%
293K	125(1)	53(2)	0.30(9)	43%	135(1)	140(3)	-0.15(9)	57%
273K	130(1)	58(1)	0.35(5)	45%	133(1)	145(3)	-0.20(5)	55%
253K	129(1)	58(2)	0.30(9)	45%	125(1)	145(2)	-0.20(9)	55%
233K	121(1)	100(2)	0.75(9)	49%	142(1)	115(3)	-0.50(5)	51%
213K	121(1)	110(2)	0.65(5)	56%	135(1)	110(5)	-0.45(5)	44%
193K	122(1)	120(2)	0.60(5)	57%	133(1)	108(3)	-0.40(3)	43%
173K	122(1)	135(3)	0.65(3)	56%	137(1)	120(4)	-0.20(5)	44%
153K	122(1)	150(2)	0.60(9)	67%	136(1)	135(2)	-0.20(5)	33%

It is interesting to note that the type of $^{13}CO_2$ motions in the UTSA-74 (1.48 $^{13}CO_2$/ Zn2) are somewhat different from those at low $^{13}CO_2$ loadings based on dynamical simulation. At the loading of 1.48 $^{13}CO_2$/ Zn2, there are two types of $^{13}CO_2$ molecules, both of which undergo a localized C_6 wobbling and a non-localized C_2 hopping motions (Figure 3-8i, 3-8ii). But the nature of and the parameters defining these motions are different. To be explicit, θ and δ are the angles that characterize the C_6 and C_2 rotation for site 1, respectively. C_6 and C_2 rotation angles for site 2 are specified by φ and η, correspondingly. Their values at different temperatures are listed in Table 3-7. As the temperature increases, the value of θ increases concomitantly from 34.0° at 153 K to 47.0° at 313 K. In comparison, at any given temperature, the C_6 wobbling angle of the $^{13}CO_2$ in the UTSA-74 (1.48 $^{13}CO_2$/ Zn2) is larger than those at the 0.30 and 0.54 $^{13}CO_2$/ Zn2, which suggests that the $^{13}CO_2$ is more mobile at the high loading (Figure 3-9). The C_2 rotation angels δ at adsorption site 1 stay consistent (25°±2°) with temperature. For site 2, both rotation angles φ and η exhibit no significant changes with temperature.

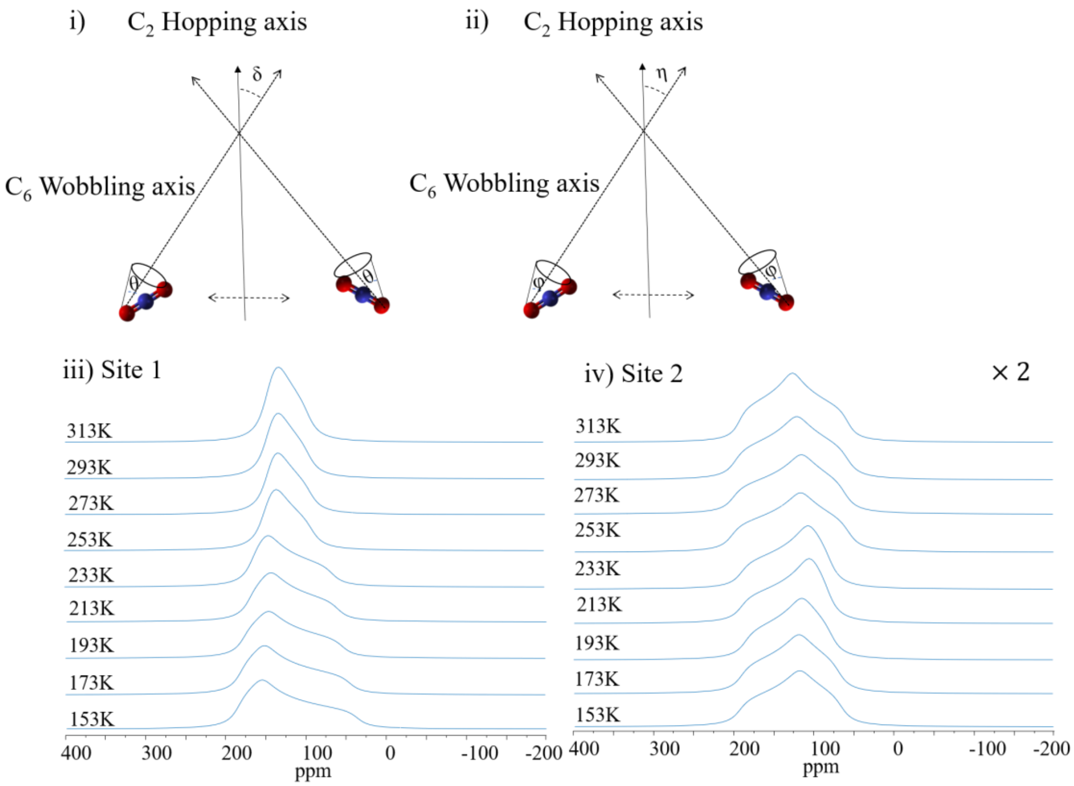

Figure 3-8: In the UTSA-74 at a loading level of 1.48 $^{13}CO_2$/ Zn2: i) CO_2 undergoes a localized C_6 wobbling with a rotation angle θ and a non-localized C_2 hopping with a rotation angle δ at site 1. ii) CO_2 undergoes a localized six-fold wobbling (C_6, φ) and a non-localized two-fold hopping (C_2, η) at site 2. Atom colors: O-Red, C-Blue. The simulated spectra of Site 1 iii) and Site 2 iv) are plotted from 153 K to 313 K using EXPRESS. The intensity of the site 2 is scaled up by a factor of 2.

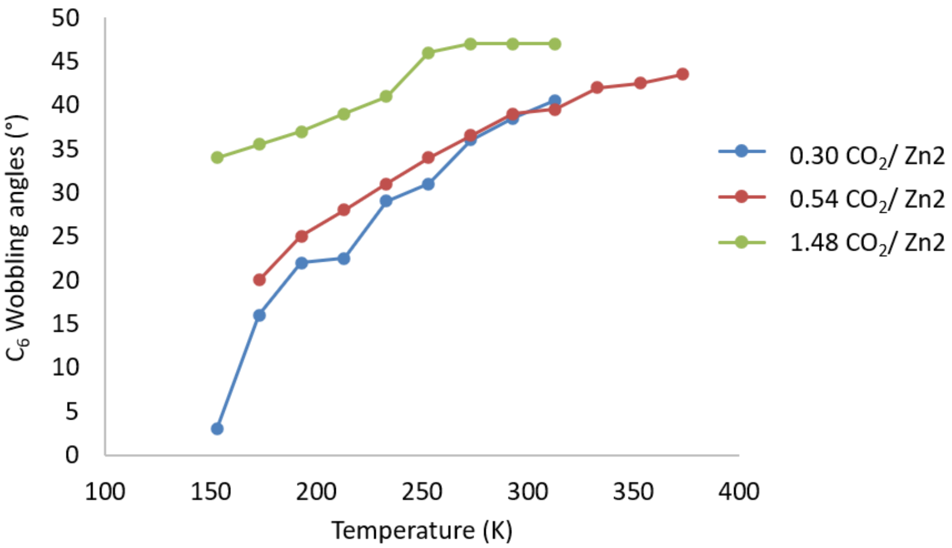

Figure 3-9: A comparison of C_6 rotation angles in the UTSA-74 at loading of 0.30, 0.54 and 1.48 $^{13}CO_2$/ Zn2 from 153 to 373 K.

Table 3-7: The rotation angles of θ, δ for site 1 and φ, η for site 2 in the UTSA-74 (1.48 $^{13}CO_2$/ Zn2) from 153 to 313 K.

	Site 1		Site 2	
Temperature(K)	C_6 (θ)	C_2 (δ)	C_6 (φ)	C_2 (η)
313K	47.0°(5)	27.0°(5)	31°(1)	35.0°(5)
293K	47.0°(5)	26.5°(5)	29°(1)	36.5°(5)
273K	47.0°(5)	25.0°(5)	28°(1)	38.0°(5)
253K	46.0°(5)	26.0°(5)	27°(1)	37.5°(5)
233K	41.0°(5)	23.5°(5)	32°(1)	41.0°(5)
213K	39.0°(5)	26.0°(5)	32°(1)	41.5°(5)
193K	37.0°(5)	26.5°(5)	34°(1)	39.0°(5)
173K	35.5°(5)	25.0°(5)	32°(1)	37.5°(5)
153K	34.0°(5)	24.0°(5)	31°(1)	37.5°(5)

In addition, it is intriguing that CO_2 molecules adsorbed at site 1 and 2 are not equivalent at the high loading even though both types of CO_2 molecules undergo C_6 wobbling and C_2 hopping motions simultaneously. This is likely due to the distorted Zn2 coordination environment. According to the study of Luo et al.[2], after Zn2 adsorption sites in UTSA-74 are fully vacated or activated, the Zn2 is in a square planar configuration (Figure 3-10i) with two open metal sites. When a single $^{13}CO_2$ molecule coordinates to the Zn2, the O=C=O adopts a distorted square pyramidal geometry with Zn2 being pulled slightly above the base plane, which is defined by four oxygen atoms from the linkers (Figure 3-10i). Provided that the five-coordinated Zn is less stable than the six-coordinated Zn, at a high $^{13}CO_2$ loading, each Zn2 tends to bind two $^{13}CO_2$ molecules. Nevertheless, the distorted square pyramidal geometry makes the bonding between Zn2 and the second $^{13}CO_2$ slightly weaker. This is because the electrostatic repulsion force between the four atoms that define the square base plane and the oxygen in the incoming $^{13}CO_2$. prevents the second $^{13}CO_2$ from binding to Zn2 very tightly. Based on the above discussion, we tentatively suggest that at a high loading level, two $^{13}CO_2$ molecules that are adsorbed at the same Zn2 have different binding strengths and are therefore inequivalent.

We further assign the two powder patterns to these inequivalent $^{13}CO_2$ molecules (Figure 3-10i). According to the interaction strength between $^{13}CO_2$ and Zn2, the $^{13}CO_2$ powder pattern designated as site 2 is assigned to the first $^{13}CO_2$ as it strongly interacts with Zn2, pulling the Zn2 above the base. The stronger interaction is reflected by the larger isotropic chemical shift. Correspondingly, the powder pattern designated as site 1 is assigned to the second physiosorbed $^{13}CO_2$ with comparatively weaker interaction, which is consistent with the larger $^{13}CO_2$ wobbling angle at site 1 in relative to that at site 2. Figure 3-10ii and iii further provide a close view of $^{13}CO_2$ non-localized C_2 hopping when each Zn2 is coordinated to two $^{13}CO_2$ at a high loading level.

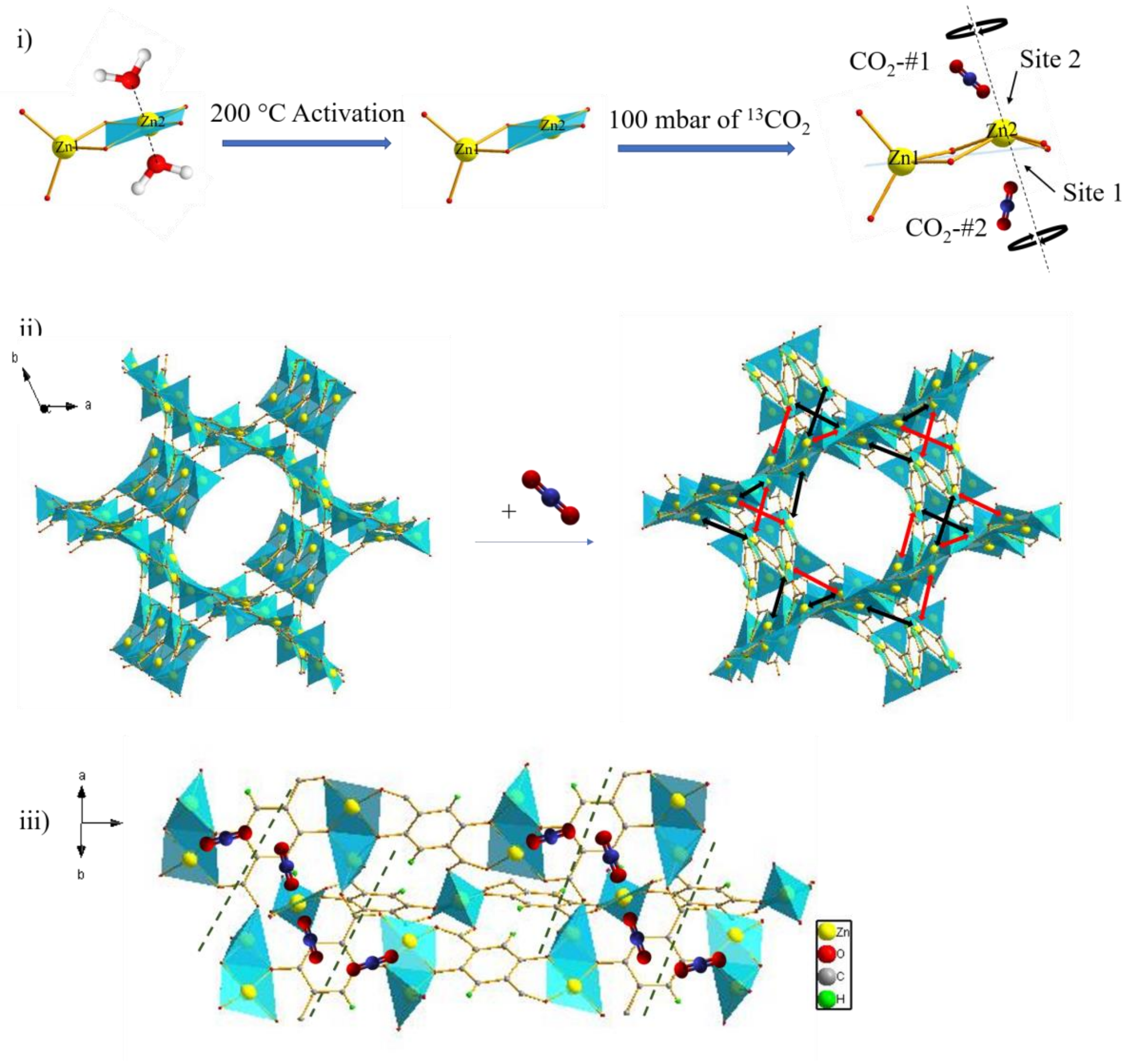

Figure 3-10: i) Illustration of $^{13}CO_2$ adsorption in the UTSA-74 at a loading level of 1.48 $^{13}CO_2$/ Zn2. In as-made MOF, each Zn2 has octahedral coordination environment with two axial positions occupied by two H_2O (solvent) molecules before samples activation. After H_2O molecules are removed by the activation, the two binding sites or open metal sites on Zn2 are produced. When 100 mbar of $^{13}CO_2$ was loaded to 110 mg of the UTSA-74, yielding a high loading level of 1.48 $^{13}CO_2$/ Zn2, every Zn2, on average, is bound to at least one $^{13}CO_2$ and many coordinate to two $^{13}CO_2$. Specifically, when the first $^{13}CO_2$ (CO_2-#1) binds to Zn2, it strongly interacts with Zn2, pulling it out of the base plane. The second $^{13}CO_2$ approaching the Zn from the bottom of the base, is denoted as CO_2-#2. Atom colors: Zn-Yellow, O-Red, C-Blue, H-White. ii) The structure of the UTSA-74 (left) showing the

empty channel and the structure of UTSA-74 loaded with $^{13}CO_2$ (right). In this diagram, the pathways of $^{13}CO_2$ molecules undergoing two different C_2 hopping motions are shown. To differentiate, the C_2 hopping at site 1 is shown by red double arrows, whereas the C_2 hopping at site 2 is shown by black double arrows. iii) A close view of $^{13}CO_2$ non-localized C_2 hopping when each Zn2 is occupied by two $^{13}CO_2$. Atom colors: Zn-Yellow, O-Red, C-Grey, H-Green, C from $^{13}CO_2$ are highlighted in blue.

Moreover, the Zn2's coordination environment is also the reason why $^{13}CO_2$ undergoes C_2 rather than C_3 hopping when sufficient amounts of $^{13}CO_2$ is available. As mentioned earlier, upon removal of two H_2O molecules by activation, the Zn2 local geometry becomes approximately square planar, which is energetically unstable[2]. Therefore, Zn2 prefers a higher coordination number for stabilization. As a result, at a low loading, a $^{13}CO_2$ molecule tends to interact with as many Zn2 as possible. By undergoing a delocalized C_3 hopping among three separated Zn2 on the channel cross-section, $^{13}CO_2$ molecules are capable to bind to more Zn2. Although C_3 hopping motion is more energy-consuming, as the path between three non-adjacent Zn2 sites in C_3 hopping (11.72 Å) is longer than that for C_2 jumping (6.79 Å), at a low loading, being able to contact with more Zn2 atoms compensates the longer travelling distance. However, when more than one $^{13}CO_2$ molecules are available for each Zn2, the demand for C_3 hopping diminishes because each Zn2 has already been occupied by one $^{13}CO_2$. Instead, C_2 hopping between two sites are energetically more favorable.

In addition, the motions of $^{13}CO_2$ at a moderate loading level is also investigated by loading 99 mbar of $^{13}CO_2$ into 180 mg of UTSA-74a, leading to the UTSA-74 with a loading level of 0.90 $^{13}CO_2$/ Zn2, close to fifty percentage of the maximum loading capacity. The experimental and simulated ^{13}C NMR spectra of the UTSA-74 (0.90 $^{13}CO_2$/ Zn2) at temperatures ranging from 133 K to 333 K are plotted in Figure 3-11i, 3-11ii. According to the simulations from WSolids, there are also two $^{13}CO_2$ adsorption sites within the MOF. (Figure 3-11iii, 3-11iv).

The analytically simulated apparent CS parameters (δ_{iso}, Ω, κ) of the UTSA-74 (0.90 $^{13}CO_2$/ Zn2) are listed in Table 3-8. For site 1, the observed value of span (Ω) steadily expands from 47 ppm to 110 ppm as the temperature decreases from 333 K to 133 K, while the skew (κ) remains consistent with little changes. Remarkably, both values of Ω and κ in the 0.90 $^{13}CO_2$/ Zn2 are smaller than those of the 0.30 and 0.54 $^{13}CO_2$/ Zn2, which imply that $^{13}CO_2$ is more mobile at the moderate loading level compared to the low loading levels. For site 2, Ω rises from 45 ppm to 110 ppm as the temperature decreases from 333 K to 153 K, while the value of κ shrinks from 0.7 to 0.12 from 313 K to 133 K. Noticeably, the population of CO_2 at adsorption site 2 is higher at lower temperatures.

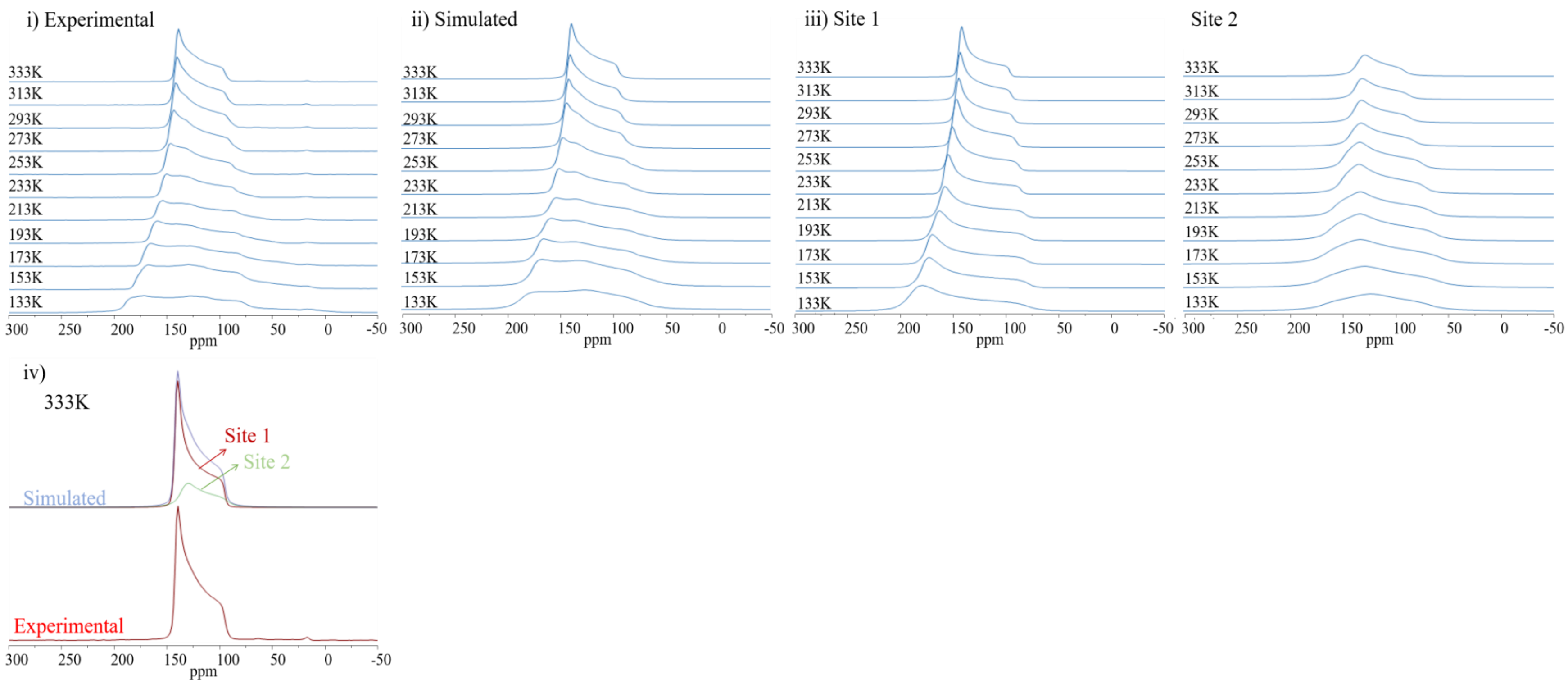

Figure 3-11: i) Experimental. ii) Simulated VT ^{13}C static NMR spectra of the UTSA-74 at a loading level of 0.90 $^{13}CO_2$/ Zn2 at temperatures ranging from 133 K to 333 K. iii) Simulated spectra of site 1 and site 2 from 133 K to 333 K using WSolids. iv) Experimental and simulated spectra of the UTSA-74 (0.90 $^{13}CO_2$/ Zn2) at 333 K and the deconvoluted components of site 1 (red) and site 2 (green).

Table 3-8: The apparent ^{13}C chemical shift parameters of $^{13}CO_2$ adsorbed at site 1 and site 2 in the UTSA-74 (0.90 $^{13}CO_2$/ Zn2) from 133 to 333 K.

	Site 1				Site 2			
Temperature(K)	iso(ppm)	Ω	κ	Site 1%	iso(ppm)	Ω	κ	Site 2%
333K	124.0(5)	47(1)	0.92(2)	74%	118.0(6)	45(2)	0.70(8)	26%
313K	124.5(5)	50(1)	0.91(2)	75%	118.0(6)	50(1)	0.80(9)	25%
293K	124.5(5)	54(1)	0.91(3)	68%	118.0(6)	53(1)	0.80(9)	32%
273K	125.5(5)	59(1)	0.89(4)	59%	118.0(4)	61(2)	0.67(7)	41%
253K	127.0(5)	65(1)	0.91(4)	44%	118.0(4)	75(1)	0.58(4)	56%
233K	129.0(5)	72(1)	0.88(2)	39%	118.0(4)	80(1)	0.55(3)	61%
213K	130.5(5)	79(2)	0.90(6)	34%	118.0(3)	92(1)	0.46(4)	66%
193K	133.5(5)	86(1)	0.90(6)	38%	118.0(5)	103(1)	0.43(3)	62%
173K	138.0(5)	94(1)	0.90(4)	38%	118.0(5)	108(1)	0.40(2)	62%
153K	140.0(5)	99(1)	0.90(6)	36%	118.0(6)	110(1)	0.28(2)	64%
133K	146.0(5)	110(1)	0.80(4)	43%	118.0(6)	101(2)	0.12(4)	57%

The $^{13}CO_2$ motions derived from EXPRESS simulation are presented in Figure 3-12 and Table 3-9. Interestingly, $^{13}CO_2$ at this loading undergoes the same types of motions as the UTSA-74 (0.3$^{13}CO_2$/ Zn2) and UTSA-74 (0.54 $^{13}CO_2$/ Zn2): At site 1, $^{13}CO_2$ undergoes a localized C_6 (α) wobbling and a non-localized C_3 (β) hopping; At site 2, $^{13}CO_2$ undergoes a C_6 (θ) wobbling and a C_2 (δ) hopping. As temperature increases from 133 K to 313 K, α and β increase from 40.5° to 47.5° and 15° to 21°, respectively. For site 2, θ increase from 38.0° at 133 K to 48.0° at 333 K.

At all three loading levels (0.90, 0.54 and 0.30 CO_2/ Zn2), the lineshape and the apparent CS parameters of site 1 as well as the motions derived from dynamical simulation are very similar, indicating that the CO_2 inside the MOF at moderate and low loadings behave the same way. Indeed, $^{13}CO_2$ at 0.90 CO_2/ Zn2 adsorption site 1 undergoes the similar types of motions because the simulated spectra for all three loading levels (0.90, 0.54 and 0.30 CO_2/ Zn2) are similar. At any given temperature, the value of α is the highest at the 0.90 $^{13}CO_2$/ Zn2, and lowest at the 0.30 $^{13}CO_2$/ Zn2, suggesting that the amplitude of $^{13}CO_2$ wobbling motion increases with increasing loading level. However, $^{13}CO_2$ at the

0.90 $^{13}CO_2$/ Zn2 adsorption site 2 presents a fairly unique powder pattern and CS parameters that are not in good agreement with the 0.30 and 0.54 $^{13}CO_2$/ Zn2. More importantly, the value of δ_{iso} at the 0.90 $^{13}CO_2$/ Zn2 adsorption 2 (i.e. 118 ppm) is small for both physiosorbed and chemisorbed $^{13}CO_2$. In this case, we cannot make any convincing assumption and more careful study at this loading is needed.

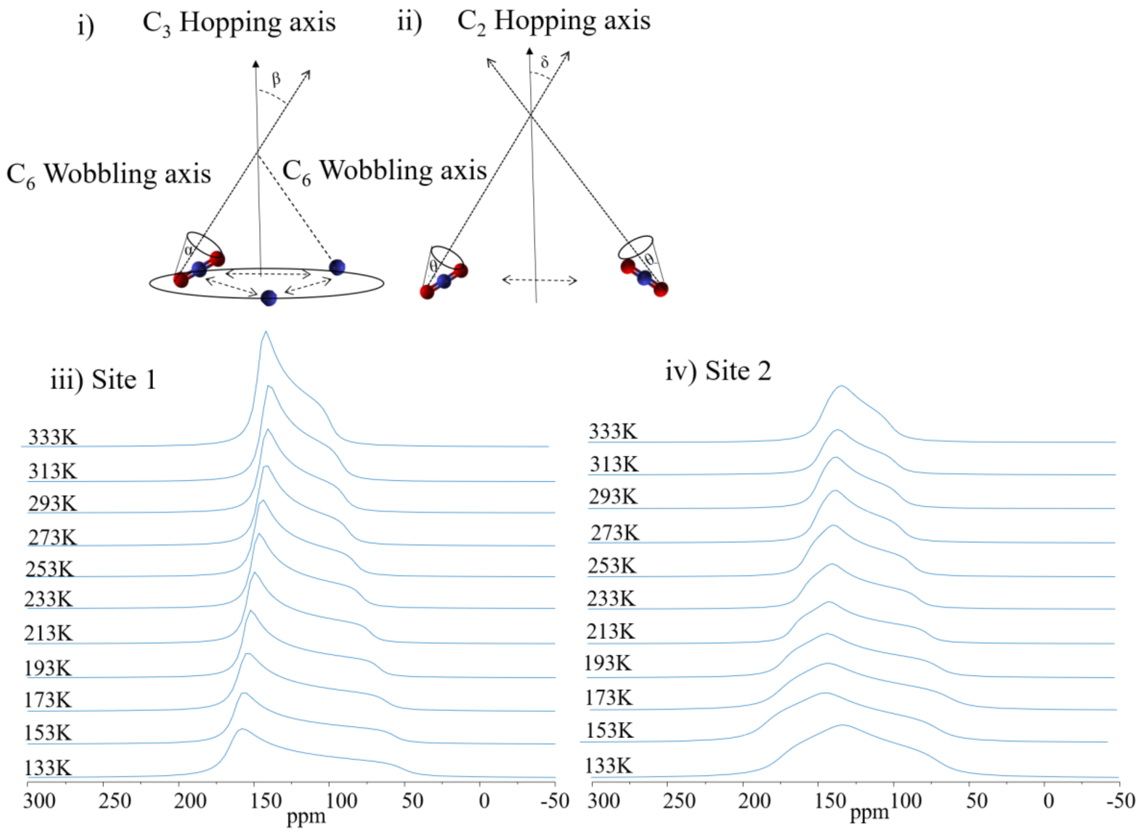

Figure 3-12: In UTSA-74 at a loading level of 0.90 $^{13}CO_2$/ Zn2: i) CO_2 undergoes a localized C_6 wobbling with a rotation angle α and a non-localized C_3 hopping with a rotation angle β at site 1. ii) CO_2 undergoes a localized six-fold wobbling (C_6, θ) and a non-localized two-fold hopping (C_2, δ) at site 2. Atom colors: O-Red, C-Blue. The simulated spectra of Site 1 iii) and Site 2 iv) are plotted from 133 K to 333 K using EXPRESS.

Table 3-9: The rotation angles of α, β for site 1 and θ, δ for site 2 in the UTSA-74 (0.90 $^{13}CO_2$/ Zn2) from 133 to 333 K.

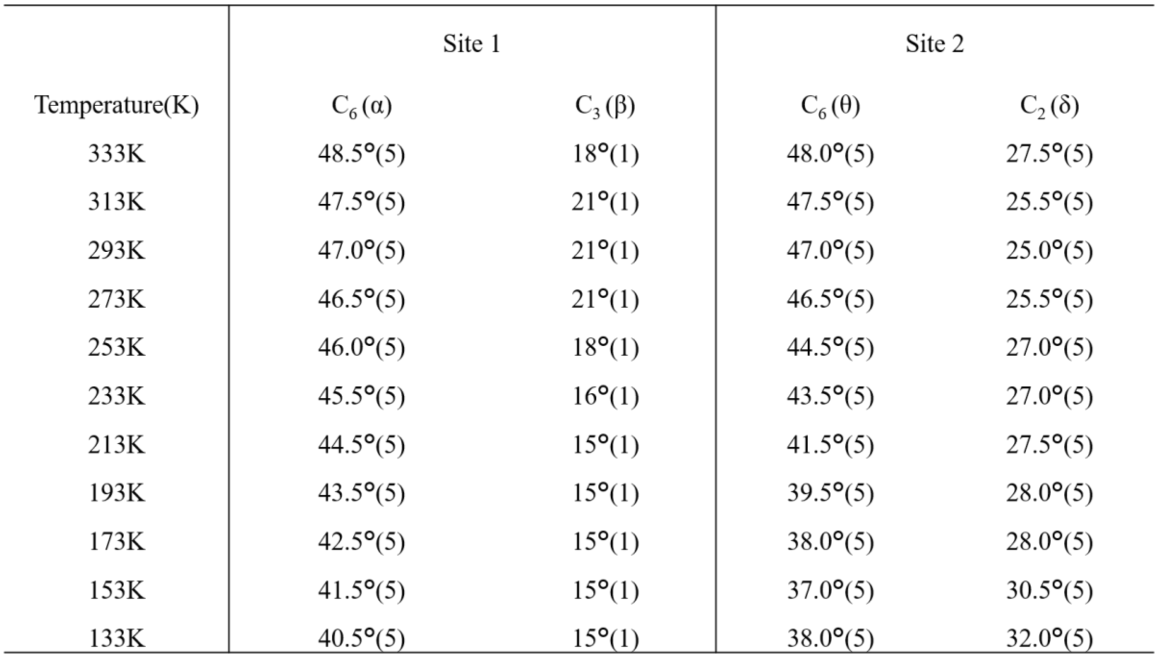

	Site 1		Site 2	
Temperature(K)	C_6 (α)	C_3 (β)	C_6 (θ)	C_2 (δ)
333K	48.5°(5)	18°(1)	48.0°(5)	27.5°(5)
313K	47.5°(5)	21°(1)	47.5°(5)	25.5°(5)
293K	47.0°(5)	21°(1)	47.0°(5)	25.0°(5)
273K	46.5°(5)	21°(1)	46.5°(5)	25.5°(5)
253K	46.0°(5)	18°(1)	44.5°(5)	27.0°(5)
233K	45.5°(5)	16°(1)	43.5°(5)	27.0°(5)
213K	44.5°(5)	15°(1)	41.5°(5)	27.5°(5)
193K	43.5°(5)	15°(1)	39.5°(5)	28.0°(5)
173K	42.5°(5)	15°(1)	38.0°(5)	28.0°(5)
153K	41.5°(5)	15°(1)	37.0°(5)	30.5°(5)
133K	40.5°(5)	15°(1)	38.0°(5)	32.0°(5)

3.3 Bibliography

1. Bueken, B.; Reinsch, H.; Heidenreich, N.; Vandekerkhove, A.; Vermoortele, F.; Kirschhock, C. E. A.; Stock, N.; Vos, D. D.; Ameloot, R. An in Situ Investigation of the Water-Induced Phase Transformation of UTSA-74 to MOF-74(Zn). *CrystEngComm* **2017**, 19 (29), 4152–4156.
2. Luo, F.; Yan, C.; Dang, L.; Krishna, R.; Zhou, W.; Wu, H.; Dong, X.; Han, Y.; Hu, T.-L.; O’Keeffe, M.; Wang, L.; Luo, M.; Lin, R.-B.; Chen, B. UTSA-74: A MOF-74 Isomer with Two Accessible Binding Sites per Metal Center for Highly Selective Gas Separation. *Journal of the American Chemical Society* **2016**, 138 (17), 5678–5684.
3. Dybowski, C.; Neue, G., Solid state ^{207}Pb NMR spectroscopy. *Progress in Nuclear Magnetic Resonance Spectroscopy* **2002,** *41* (3), 153-170.
4. Hahn, E. L. Spin Echoes. *Physical Review* **1950**, 80 (4), 580–594.
5. Beeler, A. J.; Orendt, A. M.; Grant, D. M.; Cutts, P. W.; Michl, J.; Zilm, K. W.; Downing, J. W.; Facelli, J. C.; Schindler, M. S.; Kutzelnigg, W., Low-Temperature Carbon-13 Magnetic Resonance in Solids. 3. Linear and Pseudolinear Molecules. *Journal of the American Chemical Society* **1984**, 106 (25), 7672-7676.

6. Wang, W. D.; Lucier, B. E.; Terskikh, V. V.; Wang, W.; Huang, Y. Wobbling and Hopping: Studying Dynamics of CO_2 Adsorbed in Metal–Organic Frameworks via ^{17}O Solid-State NMR. *The Journal of Physical Chemistry Letters* **2014**, *5* (19), 3360–3365.

7. Lin, L.-C.; Kim, J.; Kong, X.; Scott, E.; McDonald, T. M.; Long, J. R.; Reimer, J. A.; Smit, B. Understanding CO_2 Dynamics in Metal-Organic Frameworks with Open Metal Sites. *Angewandte Chemie* **2013**, *125* (16), 4506–4509.

8. Bertsch, L.; Habgood, H., An Infrared Spectroscopic Study of the Adsorption of Water and Carbon Dioxide by Linde Molecular Sieve X1. *The Journal of Physical Chemistry* **1963,** *67* (8), 1621-1628

9. Ward, J. W.; Habgood, H. W. The Infrared Spectra of Carbon Dioxide Adsorbed on Zeolite X. *The Journal of Physical Chemistry* **1966**, *70* (4), 1178–1182.

10. Stueber, D.; Patterson, D.; Mayne, C. L.; Orendt, A. M.; Grant, D. M.; Parry, R. W., Carbonates, Thiocarbonates, and the Corresponding Monoalkyl Derivatives. 1. Their Preparation and Isotropic ^{13}C NMR Chemical Shifts. *Inorganic Chem*istry **2001**, 40 (8), 1902-1911.

3.4 Appendices

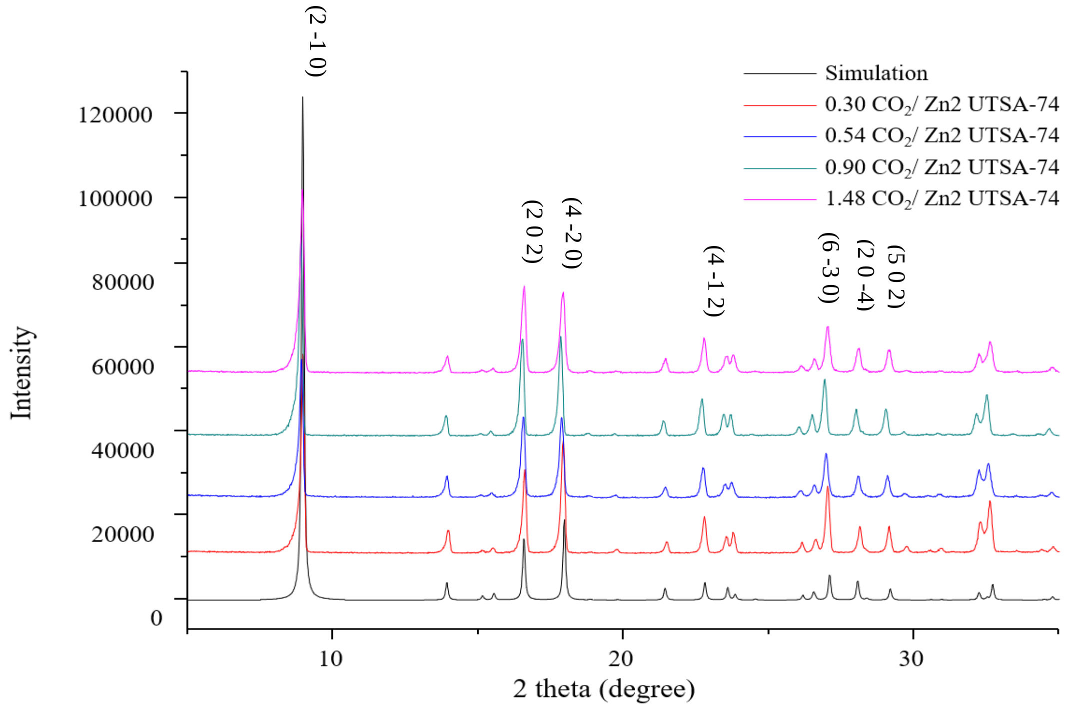

Figure S3-1: The simulated pXRD pattern calculated from the single crystal data of UTSA-74 and the experimental pXRD patterns of four as-made UTSA-74 samples. All pXRD diffractograms were acquired using a Rigaku diffractometer operating with Co Kα radiation (λ = 1.7902 Å). Diffractograms were collected at 2θ values ranging from 5 to 45 degrees with an increment of 0.02° at a scanning rate of 10°/ min. The strongest seven reflections are indexed in the pXRD. Since the experimental diffractograms are in good agreement with the simulated diffractogram of literature reported UTSA-74, this confirms that the four as-made samples are UTSA-74.

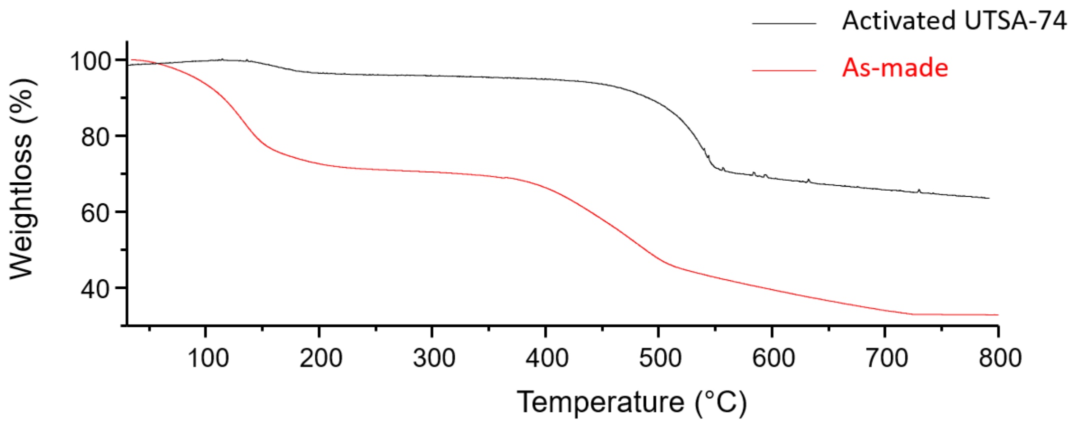

Figure S3-2: Thermogravimetric analyses of as-made UTSA-74 (red) and activated UTSA-74 (black) measured under N_2 flow using a Mettler Toledo TGA/SDTA851e instrument from 25 °C to 800 °C at a constant heating rate of 10 °C/ min. As revealed in the TGA of the as-made UTSA-74, there is a total weight loss of approximately 25% between 74 °C to 162 °C, corresponding to the removal of solvent molecules. In the activated UTSA-74, a weight loss of 3% between 133 °C to 184 °C is observed, indicating that the majority of solvent has been removed after the sample activation, while a small amount of solvent in the UTSA-74 framework remains.

Chapter 4

4 Summary and future works

4.1 Summary

In this thesis, VT ^{13}C static SSNMR experiments were carried out to investigate the behavior of CO_2 in MOF UTSA-74 at different $^{13}CO_2$ loading levels. Specifically, our study focuses on the effect of $^{13}CO_2$ loading (low, moderate, high) levels on the nature and degree of $^{13}CO_2$ motions and the interaction between $^{13}CO_2$ and UTSA-74 framework. To extract CS parameters and dynamic information of $^{13}CO_2$, two simulation software (WSolids and EXPRESS) package are employed. By simulating ^{13}C SSNMR experimental spectra using WSolids, the number of inequivalent CO_2 in the unit cell were derived at each loading and their values of δ_{iso}, Ω and κ at each experimental temperature were obtained. Simulation using EXPRESS software package yields the dynamic information on $^{13}CO_2$ molecules that are adsorbed in the MOF, such as their motion rates, modes, and motional angles.

In chapter 3, our results suggest that $^{13}CO_2$ undergoes different types of motions when different amount of $^{13}CO_2$ is loaded. Given that each Zn2 adsorption site at UTSA-74 is capable to adsorb 2 $^{13}CO_2$ molecules at maximum (i.e. 2 $^{13}CO_2$/ Zn2), we define three loading levels: A low loading level, where each Zn2 is occupied by less than 1 $^{13}CO_2$ (i.e. < 1 $^{13}CO_2$/ Zn2); A high loading level, where each Zn2 is occupied by more than 1 $^{13}CO_2$/ Zn2 (i.e. >1 $^{13}CO_2$/ Zn2) and a moderate level, where each Zn2 is bound to approximately 1 $^{13}CO_2$ (i.e. =1 $^{13}CO_2$/ Zn2).

At the UTSA-74 (0.30 $^{13}CO_2$/ Zn2) and UTSA-74 (0.54 $^{13}CO_2$/ Zn2), ^{13}C SSNMR spectra suggest that there is no free gaseous $^{13}CO_2$ in the framework and $^{13}CO_2$ exhibits reduced mobility at lower temperatures. In addition, simulations indicate that there are two adsorption sites in UTSA-74 and $^{13}CO_2$ undergoes distinct motions at each site: At site 1, $^{13}CO_2$ molecules undergo a localized C_6 wobbling around the Zn2 adsorption site and a non-localized C_3 hopping among three separated Zn2 adsorption sites on the channel cross-section (C_6+C_3). Hopping among three sites enables Zn2 to achieve higher coordination. At site 2, $^{13}CO_2$ molecules undergo a localized C_6 wobbling along with a non-localized C_2 hopping between two neighboring Zn2 (C_6+C_2). Noticeably, the interaction between $^{13}CO_2$

and Zn2 at adsorption site 2 is considered stronger than that of a typical physiosorbed $^{13}CO_2$. Similar types of motions have been observed in MOF-74-Zn, the framework isomer of UTSA-74. However, due to the difference in the number of OMS on the channel cross-section, $^{13}CO_2$ can jump among all six OMS in the channel in MOF-74-Zn (C_6 hopping), rather than among only 3 OMS in UTSA-74. Additionally, it was proposed that $^{13}CO_2$ molecules are less mobile in UTSA-74 and the adsorptive interaction between $^{13}CO_2$ and Zn2 is stronger.

At the UTSA-74 (1.48 $^{13}CO_2$/ Zn2), similarly, there are also two adsorption sites and simulations suggest that $^{13}CO_2$ undergoes a combinational C_6 wobbling and C_2 hopping motion at both adsorption sites, but CO_2 molecules at two different sites interact with the framework with different strengths. We propose that when significant amount of $^{13}CO_2$ is introduced to UTSA-74, $^{13}CO_2$ tends to undergo a combined motion of C_6 wobbling + C_2 hopping over C_6 wobbling + C_3 hopping. This is because at higher loading, Zn2 has an average coordination number greater than 5. Thus, CO_2 prefers to hop via shorter path.

Besides, static VT ^{13}C static SSNMR experiments were also conducted at UTSA-74 with a moderate loading level (i.e. 0.90 $^{13}CO_2$/ Zn2). However, we could not make any convincing proposal in regard to $^{13}CO_2$ motions based on available results.

4.2 Future work

To begin with, I would like to further investigate the dynamics of CO_2 in UTSA-74 under a moderate loading level again as the preliminary results obtained in this thesis cannot be interpreted satisfactorily. we are unable to determine what types of the motions that $^{13}CO_2$ undergoes when each Zn2 is just occupied by one $^{13}CO_2$. Thus, conducting VT ^{13}C static SSNMR experiments on another moderate $^{13}CO_2$-loaded UTSA-74 sample is planned, which allows us to understand the relation between $^{13}CO_2$ motions and loading levels better.

In addition, the adsorption selectivity of UTSA-74 is of great interest. It was previously mentioned by Luo et al.[1] that UTSA-74 is highly selective in separating C_2H_2 and CO_2 because it is capable to adsorb much larger amount of C_2H_2 over CO_2, giving rise to high gas adsorption selectivity or sieving effect. Therefore, wideline ^{2}H NMR experiments should be conducted to study the interactions of UTSA-74 with C_2D_2, the dynamics of C_2D_2 inside the framework. When both CO_2 and C_2H_2 are co-adsorbed in UTSA-74 framework simultaneously, ^{13}C and ^{2}H SSNMR results will provide key information on how UTSA-74 interacts with each adsorbate and therefore shed light on selectivity.

4.3 Bibliography

1. Luo, F.; Yan, C.; Dang, L.; Krishna, R.; Zhou, W.; Wu, H.; Dong, X.; Han, Y.; Hu, T.-L.; O'Keeffe, M.; Wang, L.; Luo, M.; Lin, R.-B.; Chen, B. UTSA-74: A MOF-74 Isomer with Two Accessible Binding Sites per Metal Center for Highly Selective Gas Separation. *Journal of the American Chemical Society* **2016**, 138 (17), 5678–5684.

Curriculum Vitae

Yingxian **Li**

Education

University of Western Ontario

London, ON

MASTER OF SCIENCE (CHEMISTRY) Sept. 2018—Present

University of Toronto

Toronto, ON

HONOUR BACHELOR OF SCIENCE Sept. 2014 –June 2018

- Specialist program in pharmaceutical chemistry.

Research Experience

Department of Chemistry, University of Western Ontario Sept. 2019-- Present

Working with Dr. Yining Huang's research group and studying the dynamics and adsorption of carbon dioxide bound to Metal-organic frameworks (MOFs) using solid-state NMR

Department of Pharmaceutical Chemistry, University of Toronto Summer 2017

Supervised by Dr. Isadore Kanfer and investigated the release profile of topical medication metronidazole from an extemporaneously prepared cream using In Vitro Release Testing.

Work Experience

University of Western Ontario

London, ON

GRADUATE TEACHING ASSISTANT

1000-Level Chemistry Courses CHEM1301, CHEM1302 Sept. 2018-April. 2020

Rexall Pharma Plus

Toronto, ON

PHARMACY ASSISTANT May 2018 –Sept. 2018

Torrance Compounding Pharmacy

Toronto, ON

PHARMACY ASSISTANT Sept. 2017 –April 2018

Summary of Course Work

CHEM9503R: Advanced NMR Spectroscopy (Quarter course, Fall 2018)

PHY 9826B: Surface Science (Half course, Winter 2019)

CHEM 9581T: Basics of Solid-state NMR (Quarter course, Winter 2019)